THE ASTROPHYSICAL JOURNAL, 611:660–684, 2004 August 20

SUBARU DEEP SURVEY. V. A CENSUS OF LYMAN BREAK GALAXIES AT $z \simeq 4$ AND 5 IN THE SUBARU DEEP FIELDS: PHOTOMETRIC PROPERTIES[1]

MASAMI OUCHI,[2,3] KAZUHIRO SHIMASAKU,[2,4] SADANORI OKAMURA,[2,4] HISANORI FURUSAWA,[5] NOBUNARI KASHIKAWA,[3] KAZUAKI OTA,[3] MAMORU DOI,[6] MASARU HAMABE,[7] MASAHIKO KIMURA,[8] YUTAKA KOMIYAMA,[5] MASAYUKI MIYAZAKI,[2] SATOSHI MIYAZAKI,[5] FUMIAKI NAKATA,[9] MAKI SEKIGUCHI,[10] MASAFUMI YAGI,[3] AND NAOKI YASUDA[3]

Received 2003 September 23; accepted 2004 April 13

ABSTRACT

We investigate the photometric properties of Lyman break galaxies (LBGs) at $z = 3.5-5.2$ based on large samples of 2600 LBGs detected in deep ($i' \lesssim 27$) and wide-field (1200 arcmin^2) images taken in the Subaru Deep Field (SDF) and the Subaru/*XMM-Newton* Deep Field (SXDF) using broadband B, V, R, i', and z' filters. The selection criteria for the LBG samples are examined with 85 spectroscopically identified objects, and the completeness and contamination of the samples are estimated from Monte Carlo simulations based on a photometric-redshift catalog of the Hubble Deep Field–North. We find that these LBG samples are nearly rest-frame UV magnitude–limited samples, missing systematically only 10% of red high-z galaxies (in number), which are a dusty population with $E(B-V) \gtrsim 0.4$. We calculate luminosity functions (LFs) of the LBGs with the estimated completeness and contamination and find (1) that the number density of bright galaxies ($M_{1700} < -22$; corresponding to SFR $\gtrsim 100\ h_{70}^{-2}\ M_\odot$ yr^{-1} with extinction correction) decreases significantly from $z = 4$ to 5 and (2) that the faint-end slope of the LFs of LBGs may become steeper toward higher redshifts. We estimate the dust extinction of $z \simeq 4$ LBGs with $M < M^*$ ($\simeq -21$) from UV-continuum slopes and obtain $E(B-V) = 0.15 \pm 0.03$ as the mean value. The dust extinction remains constant with apparent luminosity but increases with intrinsic (i.e., extinction-corrected) luminosity. We find no evolution in dust extinction between LBGs at $z = 3$ and 4. We investigate the evolution of UV-luminosity density by integrating the LFs of LBGs and find that the UV-luminosity density at 1700 Å, $\rho_{\rm UV}$, does not significantly change from $z = 3$ to 5, i.e., $\rho_{\rm UV}(z=4)/\rho_{\rm UV}(z=3) = 1.0 \pm 0.2$ and $\rho_{\rm UV}(z=5)/\rho_{\rm UV}(z=3) = 0.8 \pm 0.4$; thus, the cosmic star formation rate (SFR) density (with correction for dust extinction) remains constant within the error bars, or possibly has a slight decline, from $z = 3$ to 5. We estimate the stellar mass density from the cosmic SFR thus obtained and find that this stellar mass density is consistent with those derived directly from the stellar mass function at $z = 0$–1 but exceeds those at $z \sim 3$ by a factor of 3. We find that the ratio of the UV-luminosity density of Lyα emitters (LAEs) to that of LBGs is $\simeq$60% at $z \simeq 5$, and thus about half of star formation probably occurs in LAEs at $z \simeq 5$. We obtain a constraint on the escape fraction of UV ionizing photons (i.e., UV continuum in 900 Å) produced by LBGs, $f_{\rm esc} \gtrsim 0.13$. This implies that the escape fraction of LBGs may be larger than that of star-forming galaxies at $z = 0$.

Subject headings: cosmology: observations — galaxies: evolution — galaxies: high-redshift

1. INTRODUCTION

The formation history of galaxies is basically understood as a combination of two fundamental evolutionary processes, i.e., the production of stars and the accumulation of dark matter in the standard framework of galaxy formation, cold dark matter (CDM) models. In order to investigate the formation history of stars, one of the fundamental processes, many efforts have been made to search for high-z galaxies up to $z \simeq 7$ (Hu et al. 2002; Kodaira et al. 2003). Very deep optical to near-infrared imaging data such as the Hubble Deep Field–North (HDF-N) pioneered the detection of high-z galaxies at $z \gtrsim 3$. The photometric-redshift (photo-z) method accurately identifies the redshifts of all high-z galaxies detected in the imaging data (e.g., Connolly et al. 1995; Gwyn & Hartwick 1996; Lanzetta et al. 1996; Sawicki et al. 1997; Wang et al. 1998; Fernández-Soto et al. 1999; Benítez 2000; Fontana et al. 2000; Furusawa et al. 2000; Yahata et al. 2000; Massarotti et al. 2001; Rudnick et al. 2001). The photo-z method has an advantage in identifying high-z galaxies with little systematic selection bias. However, the photo-z method requires near-infrared images deep enough to detect faint high-z galaxies, as well as multiband optical images. Thus, application of this technique is limited to small patches of the sky and to small numbers of galaxies at relatively low redshifts ($z \lesssim 3$), because of the small field of view (FOV) of near-infrared imagers to date. On the other hand, the broadband

[1] Based on data collected at the Subaru Telescope, which is operated by the National Astronomical Observatory of Japan.

[2] Department of Astronomy, School of Science, University of Tokyo, Tokyo 113-0033, Japan; ouchi@astron.s.u-tokyo.ac.jp.

[3] National Astronomical Observatory, Mitaka, Tokyo 181-8588, Japan.

[4] Research Center for the Early Universe, School of Science, University of Tokyo, Tokyo 113-0033, Japan.

[5] Subaru Telescope, National Astronomical Observatory, 650 North A'ohoku Place, Hilo, HI 96720.

[6] Institute of Astronomy, School of Science, University of Tokyo, Mitaka, Tokyo 181-0015, Japan.

[7] Department of Mathematical and Physical Sciences, Faculty of Science, Japan Women's University, Tokyo 112-8681, Japan.

[8] Department of Astronomy, Kyoto University, Sakyo-ku, Kyoto 606-8502, Japan.

[9] Department of Physics, University of Durham, South Road, Durham DH1 3LE, UK.

[10] Institute for Cosmic Ray Research, University of Tokyo, Kashiwa, Chiba 277-8582, Japan.

two-color selection technique successfully identifies a large number of high-z galaxies detected only in optical bands, which is based on Lyman break (912 Å) features redshifted to optical wavelengths (e.g., Steidel et al. 1996a, 1996b, 1999; Madau et al. 1996, 1998; Lowenthal et al. 1997). High-z galaxies found by this method are called Lyman break galaxies, or LBGs. There are a few thousand photometrically selected high-z ($2 \lesssim z \lesssim 4$) galaxies, and about 1000 galaxies have been spectroscopically confirmed to really be located at $z \simeq 3$ (Steidel et al. 2003). The Lyman break technique is an ideal method for selecting a large number of high-z galaxies and for studying their general properties in a limited telescope time, since the method requires optical images in only a few bandpasses. Furthermore, the relative sensitivities in optical bands are better than those in near-infrared, and thus the Lyman break technique can identify higher redshift ($z \gtrsim 4$) galaxies than the photo-z method. A problem is that LBGs are generally UV-continuum–bright galaxies, since they are identified by their strong Lyman breaks. It is thought that some high-z galaxies escape from the Lyman break selection (e.g., Pascarelle et al. 1998; Dickinson 2000; Franx et al. 2003). Care is needed when we discuss the properties of high-z galaxies using LBG samples.

The luminosity functions (LFs) of high-z galaxies are obtained to reveal their number density and star formation history (e.g., Sawicki et al. 1997; Fernández-Soto et al. 1999; Furusawa et al. 2000; Poli et al. 2001; Kashikawa et al. 2003, hereafter Paper III). Steidel et al. (1999) find from their large LBG samples that the LF of LBGs at $z = 3$ is well fitted by the Schechter function with a steep slope, $\alpha = -1.6$, down to $L \simeq 0.1L^*$ and that the UV-luminosity density derived by integrating the LF does not change from $z = 3$ to $z = 4$. Thus, the cosmic star formation rate (SFR) estimated from the UV-luminosity density does not significantly drop at $z \gtrsim 3$, which is different from the early report given by Madau et al. (1996) with HDF-N galaxies. A similar tendency in the cosmic SFR is also reported by Iwata et al. (2003), who derive the cosmic SFR at $z = 5$. Here, dust extinction is a critical issue in estimating the cosmic SFR from the UV-luminosity density.

Dust extinction of LBGs at $z \sim 3$ has been estimated by Steidel et al. (1999), Meurer et al. (1999), Adelberger & Steidel (2000), and Vijh et al. (2003; see also Calzetti 2001 for review) from UV spectral slopes of LBGs. These authors show that the average (or median) dust extinction of LBGs at $z \sim 3$ is $E(B-V) = 0.10-0.30$, assuming the dust attenuation law of Calzetti et al. (1994) or Calzetti et al. (2000). Global spectral fitting from rest-frame UV to optical SEDs of LBGs at $z \sim 3$ supports this value (Sawicki & Yee 1998; Ouchi et al. 1999; Shapley et al. 2001; Papovich et al. 2001). Near-infrared spectroscopy has also yielded similar values of dust extinction using the Balmer decrement (e.g., Pettini et al. 1998, 2001, 2002). Since the dust-extinction correction for the UV luminosity ranges from a factor of 3 to 19 (presented in Vijh et al. 2003 and references therein), it is a key to determining dust extinction accurately, so as to estimate the real SFR from the UV-luminosity density.

Measuring the stellar mass density (Brinchmann & Ellis 2000; Cole et al. 2001; Cohen 2002; Dickinson et al. 2003) is an independent check for cosmic SFR measurements, since the cosmic SFR is a derivative of the stellar mass density with respect to cosmic time. Dickinson et al. (2003) have derived the stellar mass density as a function of redshift up to $z = 3$. They have found that the stellar mass density at $z = 3$ is about 6% of that in the present epoch. However, the stellar mass density at $z = 3$ that they have estimated is less than that derived by integrating the cosmic SFR given by Steidel et al. (1999) (see Cole et al. 2001), where the cosmic SFR at high redshift ($5 \lesssim z \lesssim 7$) is an extrapolation from measurements at $z \lesssim 4$. It is important to obtain accurate cosmic SFRs at $z \gtrsim 5$ and examine the cause of the discrepancy. High-z galaxies produce far-UV photons by their star formation activity, and these far-UV photons contribute to the ionization of the universe (e.g., Madau et al. 1999). Thus, it is also important to measure the star formation activity of high-z galaxies and investigate the relationship between galaxies and the reionization of the universe.

Observational studies of galaxies at $z \gtrsim 4$ were mainly based on data of the HDF-N and HDF-S, both of which have sizes of only $\sim$4–5 arcmin^2 (about $2' \times 2'$), corresponding to 4×4 Mpc^2 at $z = 4$ (comoving units), i.e., cluster scales in the present-day universe. Surveys based on such a small area probably suffer from cosmic variance, i.e., spatial inhomogeneities of galaxy properties in the universe. Cosmic variance is thought to be one of the major ambiguities in the measurements of the LF, luminosity density, SFR, etc. Furthermore, small-field surveys do not provide clustering properties of galaxies on large scales that reflect the properties of dark matter in galaxies, i.e., the other fundamental properties of galaxies.

In order to address the issues described above, we carry out deep and wide-field surveys for high-z galaxies with the Subaru Prime Focus Camera (Suprime-Cam; Miyazaki et al. 2002), which is a wide-field ($34' \times 27'$) optical imager mounted on the 8 m Subaru. We made deep and wide-field imaging for two blank fields during the Guaranteed Time Observations (GTOs) of Suprime-Cam.

One blank field is the Subaru Deep Field (SDF: R.A. = $13^h24^m21\overset{s}{.}4$, decl. = $+27°29'23''$ [J2000.0]; Maihara et al. 2001, hereafter Paper I; Ouchi et al. 2003, hereafter Paper II; Paper III; Shimasaku et al. 2003, hereafter Paper IV), and the other is the Subaru/*XMM-Newton* Deep Field (SXDF: R.A. = $02^h18^m00^s$, decl. = $-5°00'00''$ [J2000.0]; K. Sekiguchi et al. 2004, in preparation; see also Ouchi et al. 2001). These fields have little Galactic extinction and few bright stars over 1 deg^2. Thus, these fields are suitable for studying high-z galaxies by deep observations with Suprime-Cam. These two blank fields, SDF and SXDF, have also been observed in two Subaru Observatory key projects. One is the SDF project (Kashikawa et al.). The SDF project makes very deep observations for the SDF with the Suprime-Cam, multislit spectrographs (e.g., Subaru FOCAS; Kashikawa et al. 2002), and near-infrared cameras and spectrographs (e.g., Subaru CISCO; Motohara et al. 2002) to study galaxy evolution at $z = 3-7$. The area surveyed in the SDF project is about 0.2 deg^2, corresponding to one FOV of Suprime-Cam. The other is the Subaru/*XMM-Newton* Deep Survey (SXDS) project (Sekiguchi et al.). The SXDS project is a wide-field multiwavelength survey project. The field surveyed by Suprime-Cam in the SXDS project is about 1 deg^2, corresponding to 5 FOVs of Suprime-Cam. The SXDF is observed by many instruments at various wavelengths: radio with the Very Large Array, submillimeter with the James Clerk Maxwell Telescope SCUBA, infrared with SIRTF, near-infrared with the UKIRT WFCAM, optical with the Subaru Suprime-Cam and Subaru FOCAS, UV with GALEX, and X-ray with *XMM-Newton*. This paper is based on the GTO data alone, which were taken in 2000 and 2001. Deeper images (3–10 hr for each band) have been obtained in the key projects, but reduction of them is still under way.[11]

In this paper, we make large samples of LBGs at $z = 4$ and 5 with the deep and wide-field SDF+SXDF data (§§ 2–3). We derive LFs of LBGs from the large LBG samples and investigate the evolution of the LF (§ 4). We calculate dust extinction for our LBGs at $z = 4$ and examine the evolution of dust extinction for star-forming galaxies over $z = 0$–4.5 (§ 5). We calculate the UV-luminosity density of LBGs at $z = 4$ and 5 and investigate the cosmic SFR, the stellar mass density, and the escape fraction of far-UV photons from LBGs (§ 6), where we use the dust extinction of LBGs obtained in § 5. We present the clustering properties of these LBGs in a companion paper (Ouchi et al. 2004, hereafter Paper VI). In Paper VI, we combine the results of the clustering properties with those of the photometric properties shown in this paper using CDM models and give a more detailed discussion.

Throughout this paper, magnitudes are in the AB system (Oke 1974; Fukugita et al. 1995). The values for the cosmological parameters adopted in this paper are $(h, \Omega_m, \Omega_\Lambda, \Omega_b h^2) = (0.7, 0.3, 0.7, 0.02)$. These values are the same as those obtained from the latest cosmic microwave background observations (Spergel et al. 2003).

2. OBSERVATIONS AND DATA REDUCTION

2.1. *Observations*

2.1.1. *Imaging*

During the commissioning runs of Suprime-Cam (2000 November–2001 November), we carried out multiband, deep and wide-field optical imaging in two blank fields. One was the SDF (R.A. $= 13^h24^m21\overset{s}{.}4$, decl. $= +27°29'23''$ [J2000.0]; Paper I), and the other was the SXDF (R.A. $= 02^h18^m00^s$, decl. $= -5°12'00''$ [J2000.0]). The central 4 arcmin^2 region of the SDF has very deep J and K' data (Paper I). Although the central position of the SXDF is R.A. $= 02^h18^m00^s$, decl. $= -5°00'00''$ (J2000.0) (M. Sekiguchi et al. 2004, in preparation), since some bright stars are located in the neighborhood of the central position, we chose a southern part of the SXDF that is apart from the center by $12'$ for our observations. We observed these two blank fields in the B, V, R, i', and z' filters, which cover the whole optical wavelength range (4000–10,000 Å). Figure 1 shows the response of the filters used in these observations. The response includes atmospheric absorption, quantum efficiency, and transmittance of the optical elements of Suprime-Cam.

The total exposure times range from 81 to 210 and 40 to 177 minutes among the filters in the SDF and SXDF, respectively. The 3 σ limiting magnitudes are $i' = 26.9$ and $i' = 26.2$ for the SDF and SXDF, respectively. During the observations, the seeing size varied from $0\overset{''}{.}5$ to $0\overset{''}{.}9$ and $0\overset{''}{.}5$ to $1\overset{''}{.}0$ for the SDF and SXDF. Table 1 summarizes the observations. We show pseudocolor images of the SDF and SXDF in Figures 2 and 3. Although the FOV of Suprime-Cam is 918 arcmin^2 ($27' \times 34'$), only nine CCDs were installed (i.e., CCD w93c2 had not been installed; see Miyazaki et al. 2002 for positions of the CCD chips) before 2001 March.[12] In addition, CCD w67c1, installed in 2001 April, showed strong fringes, and we do not use the data taken by this CCD.[13] Neither do we use the low signal-to-noise ratio (S/N) regions located around the edge of the FOV, which are caused by dithering observations. After we reject these bad areas, the SXDF image has 653 arcmin^2 for all bandpasses. Similarly, the SDF image has 616 arcmin^2 for the B, V, i', and z' bands and 543 arcmin^2 for the R band (see Table 1).

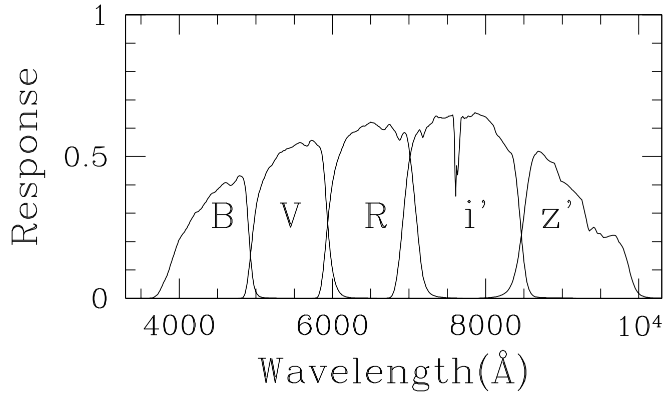

FIG. 1.—Response of the broadband filters (B, V, R, i', and z') that we used for the imaging observations.

During the observations, we took images of photometric standard stars SA92 and SA95 (Landolt 1992) in the B, V, and R bands and spectrophotometric standard stars SA95-42 and Hz44 (Oke 1990) in the i' and z' bands. These standard stars were observed a few times a night, when the night was thought to be photometric.

2.1.2. *Spectroscopy*

Spectroscopic redshift data are important for checking our selection criteria for LBGs. We carried out spectroscopic follow-up observations of LBGs detected in our data with FOCAS (Kashikawa et al. 2002) on Subaru on 2002 June 6. We used one multislit mask containing slits for four LBG candidates. We also observed five objects selected by other criteria, including Lyα emitter (LAE) candidates at $z = 4.9$ (Paper IV). Thus, the number of galaxies for which we took spectra was $4 + 5 = 9$. We chose the 300 line mm^{-1} grating with a dispersion of 1.4 Å pixel^{-1} and a wavelength coverage of 4700–9400 Å. The sensitivity decreases in blue wavelengths ($\lesssim$6000 Å; see Kashikawa et al. 2002). We adopted a slit width of $0\overset{''}{.}8$, which gave a spectral resolution of 9.8 Å. We made a 2 hr exposure for each object. The seeing size of the night was $0\overset{''}{.}7$–$0\overset{''}{.}8$. The continuum flux limit of our spectra was 6.3×10^{-19} ergs s^{-1} cm^{-2} Å^{-1} with a 5 σ significance level. In addition to these nine spectra, we use 76 spectra given by Paper III that were taken during the GTOs of FOCAS in 2001. The details of the spectra are described in § 3.1.

2.2. *Data Reduction*

We developed the pipeline software SDFRED (Paper II) to reduce Suprime-Cam data. The core programs of SDFRED are taken from IRAF, SExtractor (Bertin & Arnouts 1996), and

[11] Part of the GTO data are now included in the data of the SDF key project; e.g., about one-third of the i' and z' data presented in Kodaira et al. (2003) were taken in the GTOs.

[12] In Fig. 2 the region in the lower right corner surrounded by the dashed line and the solid line corresponds to the position of the w93c2 CCD. In Fig. 3 the upper right corner, for which no data exist, also corresponds to the position of w93c2.

[13] In Fig. 2 the region in the lower left corner corresponds to the position of the w67c1 CCD.

TABLE 1

Journal of Observations

Field Name	Band	Observed Dates	Area (arcmin^2)	Total Exposure Time (minutes)	$m_{\rm lim}$
SDF	B	2001 Apr 24–25, May 20	616	210	27.8
SDF	V	2001 Apr 23, May 20	616	150	27.3
SDF	R	2001 Mar 21–23	543	90	27.1
SDF	i'	2001 Apr 24, Mar 19, Jun 23–24	616	138	26.9
SDF	z'	2001 May 19–20, Jun 25	616	81	26.1
SXDF	B	2000 Nov 24–25	653	177	27.6
SXDF	V	2000 Nov 26–27	653	84	26.5
SXDF	R	2000 Nov 22, 24, 2001 Nov 16	653	118	27.2
SXDF	i'	2000 Nov 25	653	45	26.2
SXDF	z'	2001 Oct 14, 18, 19	653	40	25.7

Notes.—These data were taken in 2000 and 2001 during the GTOs of Suprime-Cam. Although deeper imaging (3–10 hr for each band) was carried out for both fields in 2002 and 2003 by the Subaru Observatory key projects (e.g., Kodaira et al. 2003; see § 1), the results presented in this paper are based on the GTO data only.

mosaic-CCD data reduction software (Yagi et al. 2002). SDFRED includes a set of optimized parameters that are common to any Suprime-Cam data, and it accepts free parameters dependent on the conditions of the data. This pipeline software is open to the public, and a manual of the software and instructions for installation are given in Ouchi 2003. We reduced all the observed data of good quality with SDFRED and made stacked images for all bandpasses.

We aligned these stacked images using hundreds of stellar objects in each image. Then, we smoothed the images with Gaussian kernels to match their seeing sizes. The final images have a point-spread function (PSF) FWHM of 0\.9 (SDF) and 0\.98 (SXDF).

2.2.1. *Photometric Zero Points*

We calculated photometric zero points from photometry of standard stars with a $10''\phi$ aperture (hereafter ϕ indicates the diameter of a circular aperture). We used the zero points obtained in photometric nights with air-mass correction (Ouchi et al. 2001). We checked these photometric zero points using the colors of 175 Galactic stars calculated from spectra given in Gunn & Stryker (1983). Since the FOV of Suprime-Cam is large enough to detect more than 100 bright stars with $i' \lesssim 23$, we can examine the photometric zero points using various two-color diagrams. We find that the colors of stellar objects in our data are consistent with those of the stars of Gunn & Stryker, except for some two-color diagrams in which an offset of $\simeq$0.05 mag is seen. Such offsets are probably due to photometric errors of standard stars observed in slightly nonphotometric conditions. We correct the zero points by about $\simeq$0.05 mag, so that the observed colors of stellar objects match the synthetic colors of the stars of Gunn & Stryker. The photometric zero points thus obtained are regarded as more accurate than 0.05 mag.

2.2.2. *Photometric Catalogs*

Source detection and photometry are performed using SExtractor, version 2.1.6 (Bertin & Arnouts 1996). We measure both MAG_AUTO of SExtractor and $2''\phi$ aperture magnitudes; a $2''\phi$ aperture diameter is twice as large as the seeing size, i.e., 1\.8 and 2\.0 for the SDF and SXDF data, respectively. In order to obtain faint PSF-like objects with a good S/N, we do not adopt MAG_AUTO values as the total magnitudes. Instead, we use $2''\phi$ aperture magnitudes after applying an aperture correction of 0.2 mag. We present in § 3.1 the difference between MAG_AUTO and $2''\phi$ aperture magnitudes after aperture correction. We make i'- and z'-detection catalogs for both the SDF and SXDF data. We limit the catalogs to $i' < 26.5$ and $z' < 26.0$ ($i' < 26.0$ and $z' < 25.5$) for the i'- and z'-detection catalogs of the SDF (SXDF), in order to provide a reasonable level of photometric completeness. These limiting magnitudes are defined for a $2''\phi$ diameter aperture. Our i'- and z'-detection catalogs contain 45,923 (39,301) and 37,486 (34,024) objects for the SDF (SXDF), respectively. We correct the magnitudes of objects for Galactic extinction, $E(B-V) = 0.019$ and $E(B-V) = 0.020$ (Schlegel et al. 1998), for the SDF and SXDF, respectively.

We measure 3 σ limiting magnitudes of the images, which are defined as the 3 σ levels of sky noise on a $2''\phi$ diameter. For each image, we measure sky counts in a number of $2''\phi$ apertures that are located at randomly selected positions in the image. Then, we draw a histogram of the sky counts and fit a Gaussian function to the histogram to obtain the 1 σ noise. When we fit a Gaussian function, we omit the positive tail of the histogram, which is affected by objects. The limiting magnitudes are presented in Table 1. Note that we do not simply calculate the 3 σ limiting magnitudes by scaling the 1 σ noise in 1 pixel to a $2''$ diameter area. Since this simple scaling results in a very optimistic limiting magnitude, as discussed in Furusawa (2002) and Labbé et al. (2003), we use the real noise values measured in $2''\phi$ apertures.

2.2.3. *Astrometry*

Since we correct geometric distortion of images through the data reduction, relative astrometry is good enough for this work. Relative error is less than 1 pixel (0\.202 pixel^{-1}). However, we need to obtain absolute astrometry for follow-up spectroscopy. We calibrate coordinates of objects using faint objects ($B = 19-20$) given in the USNO-A2.0 catalog (Monet 1998). Although the positional accuracies of USNO objects are not very good (typically 0\.25), there are no other calibrators that are faint enough (so that they are not saturated in our images). We use 136 and 97 USNO objects that are not saturated in the B-band image in the SDF and SXDF, respectively. They are uniformly distributed over the images. We obtain the absolute coordinates of our objects with these USNO objects. The errors in the absolute positions of objects

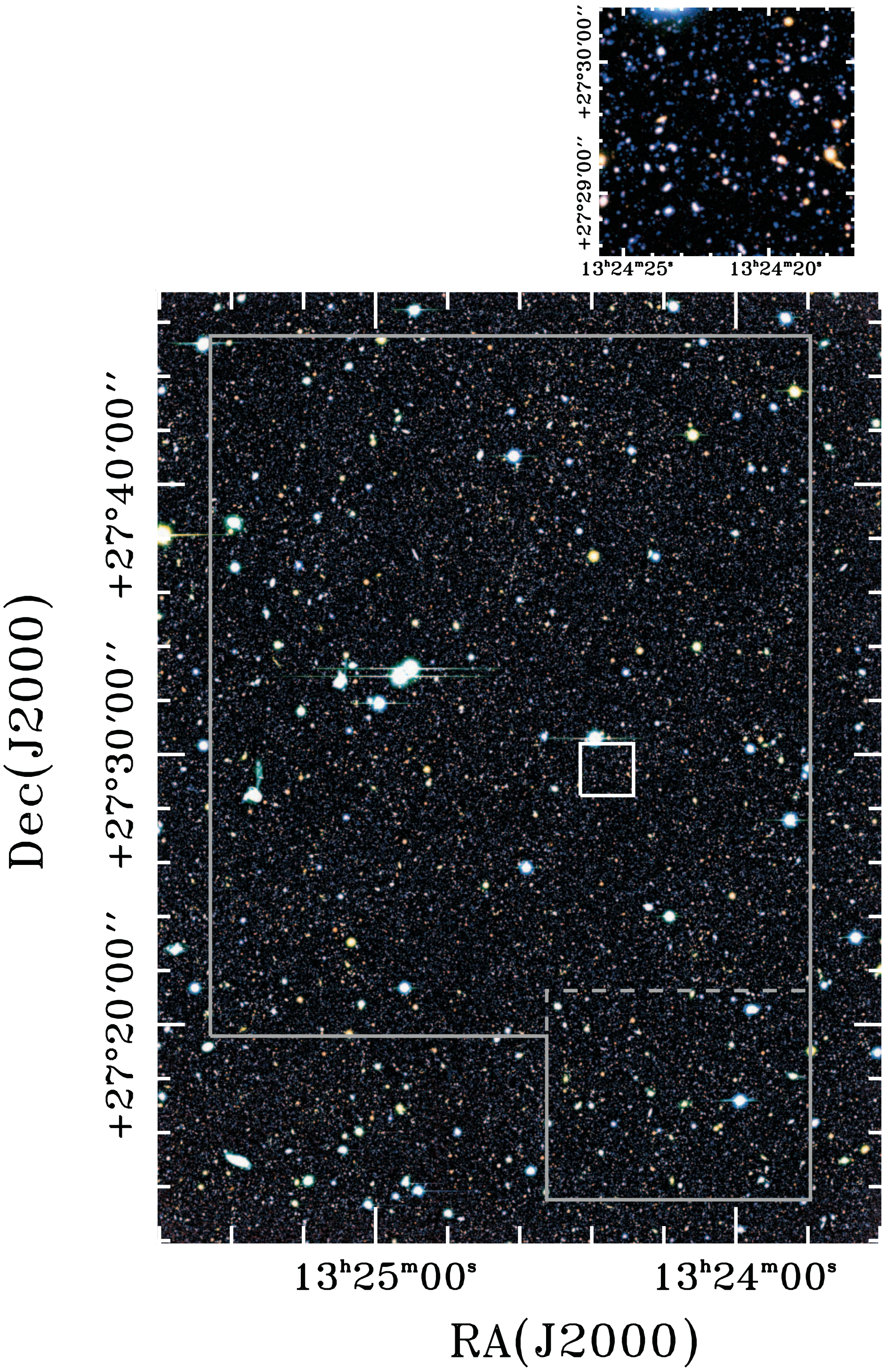

FIG. 2.—Composite pseudocolor image of the SDF. The RGB colors are assigned to the z', i', and B images, respectively. The square outlined by the white line near the center of the image is the field where deep near-infrared J and K images were obtained by Subaru CISCO (Paper I). A magnified image of this field is shown in the top right panel. The gray solid line indicates the 616 arcmin^2 area with good S/N in all bands except for the R band. We use this area for detecting *Viz*-LBGs. The gray dashed line corresponds to the border of good and bad S/N regions in the R band. The R-band data do not have good S/N below the gray dashed line, and we use the remaining 543 arcmin^2 field for detecting *BRi*-LBGs and *Riz*-LBGs. The 543 arcmin^2 field is also the field where we detect 87 LAEs at $z = 4.86$, as described in Paper II.

in (α, δ) are estimated to be less than 0\".3–0\".4 in both the SDF and the SXDF.

3. PHOTOMETRIC SAMPLES OF LBGs AT $z = 3.5$–5.2

3.1. *Definitions of BRi-, Viz-, and Riz-LBGs*

We make three photometric samples of LBGs by the following two-color selections. The first sample is for LBGs at $z \simeq 4$ selected by $B - R$ versus $R - i'$. They are referred to as *BRi*-LBGs. *BRi*-LBGs are galaxies whose Lyman break enters into the B band and whose flat UV continuum is sampled in the R and i' bands, and these galaxies are identified by their red $B - R$ and blue $R - i'$ colors. Similarly, the second is for LBGs at $z \simeq 5$ selected by $V - i'$ and $i' - z'$, and we refer to them as *Viz*-LBGs. The third is for LBGs at $z \simeq 5$ selected by $R - i'$ and $i' - z'$, and we refer to them as *Riz*-LBGs.

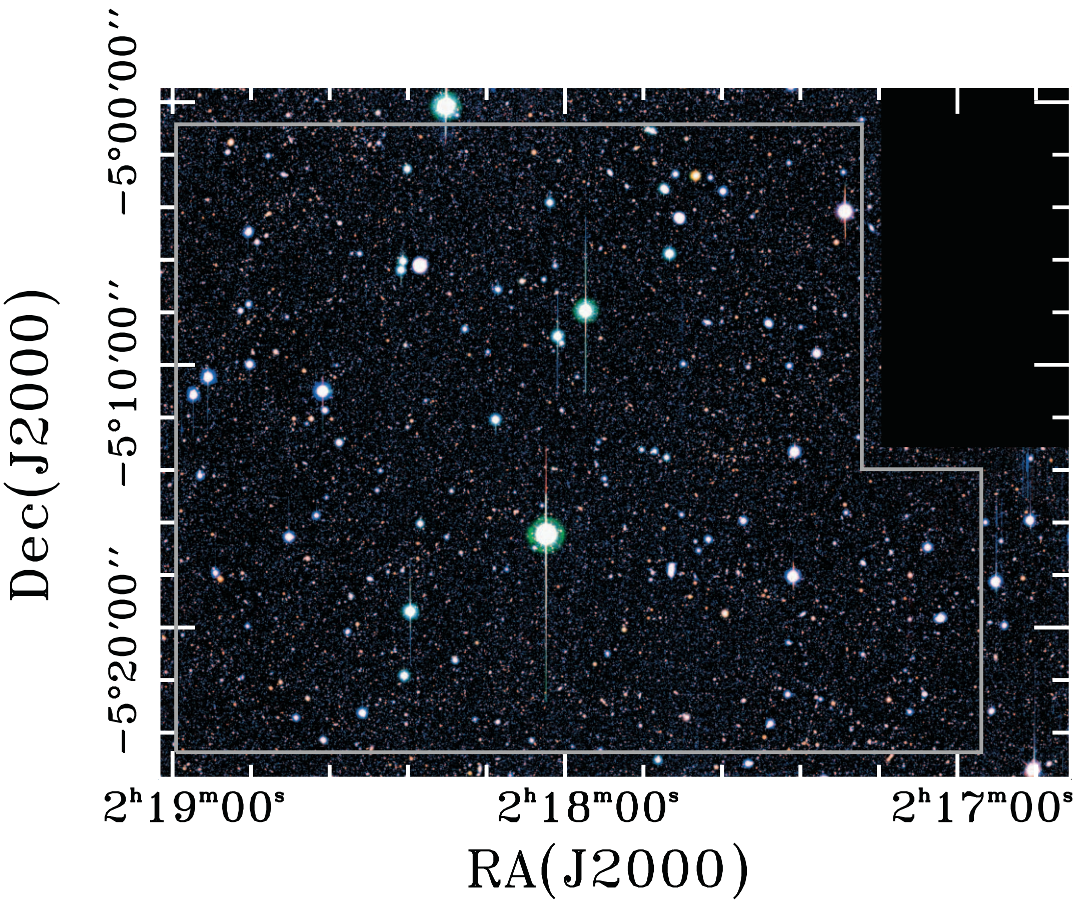

FIG. 3.—Composite pseudocolor image of the SXDF. The RGB colors are assigned to the z', i', and B images, respectively. The gray solid line indicates the 653 arcmin^2 area with good S/N.

For $z \gtrsim 4$ objects, the UV continuum shortward of 1216 Å is damped by the Lyα absorption of the intergalactic medium (IGM). Since the depression at 1216 Å is as strong as that at 912 Å (Lyman break) for galaxies at $z \gtrsim 4$, LBGs identified by the above two-color selections are not "Lyman break" galaxies but "Lyman break + Lyα absorption" galaxies in reality. The central redshift of these samples is shifted toward redshifts lower than the one calculated by dividing the central wavelength of the bluest band by 912 Å. For example, *Riz*-LBGs are expected to be located at around $z \sim 6500/912 - 1 = 6.1$, but the actual redshifts are $z \sim 5$ (§ 3.2).

Figures 4–6 illustrate how to isolate LBGs from foreground objects, including Galactic stars. These figures indicate that LBGs can be isolated from low-z galaxies and Galactic stars by their red break colors ($B - R$, $V - i'$, and $R - i'$) and their blue continuum colors ($R - i'$, $i' - z'$, and $i' - z'$). In order to define the selection criteria for LBGs quantitatively and estimate the sample completeness and contamination, we use 85 spectroscopically identified objects in our fields and 1048 galaxies in the photo-z catalog of HDF-N given by Furusawa et al. (2000), as explained in the following.

Our 85 spectroscopically identified objects come from two sources. One is the sample of nine objects for which we carried out spectroscopic follow-up observations, and the other is the spectroscopic catalog of 76 SDF objects compiled by Paper III. The nine spectra are of (1) four LBG candidates whose colors are close to those of model galaxies at $z > 3.5$ (Figs. 4–6) and (2) five objects, including the LAE candidates of Paper II (see Paper IV). We identify that these four LBG candidates are real LBGs at $z = 4.140$, 4.250, 4.270, and 4.865. (These are SDF J132413.3+274207, SDF J132416.3+274355, SDF J132413.1+274116, and SDF J132410.5+274254 in Fig. 7.) In the 76 spectra, there are two LBGs at $z > 3.5$: $z = 3.845$ and 4.600.[14] In summary, we have 85 (=9 + 76) spectroscopically identified objects at $0 \leq z < 5$, and six among them are found to be LBGs at $z > 3.5$. Out of the rest (79 objects), three are LBGs at $3.0 < z < 3.5$, four are LAEs at $z = 4.9$ that are only detected in a narrowband image (Paper II), and the other 72 objects are either blue dwarf galaxies with emission lines, red late-type galaxies up to $z = 1.1$, or late-type Galactic stars. Figure 7 shows the spectra and snapshots of the identified six LBGs, and Table 2 summarizes their properties.

We compare the colors of galaxies in our LBG samples with the colors of the 85 spectroscopically identified objects. The 85 spectroscopically identified objects are plotted on the two-color diagrams in Figures 8–10; blue circles are for interlopers and red circles are for LBGs at $3.5 < z < 4.5$, $4.2 < z < 5.2$, and $4.6 < z < 5.2$ for *BRi*-LBGs, *Viz*-LBGs, and *Riz*-LBGs, respectively. As expected, spectroscopically identified high-z galaxies are located in the top left part of the two-color diagrams. We define the selection criteria for LBGs to select

[14] The original catalog of Paper III has four LBGs at $z > 3.5$. However, one galaxy at $z = 4.620$ has spectroscopic features similar to late-type stars. Furthermore, the magnitude of this object is bright, $z' = 23.66$, and its profile is stellar. Therefore, we regard this object as a Galactic star. Another LBG at $z = 3.810$ is blended in our image, and we cannot detect this LBG as a single object. Thus, we use the remaining two LBGs for our analysis.

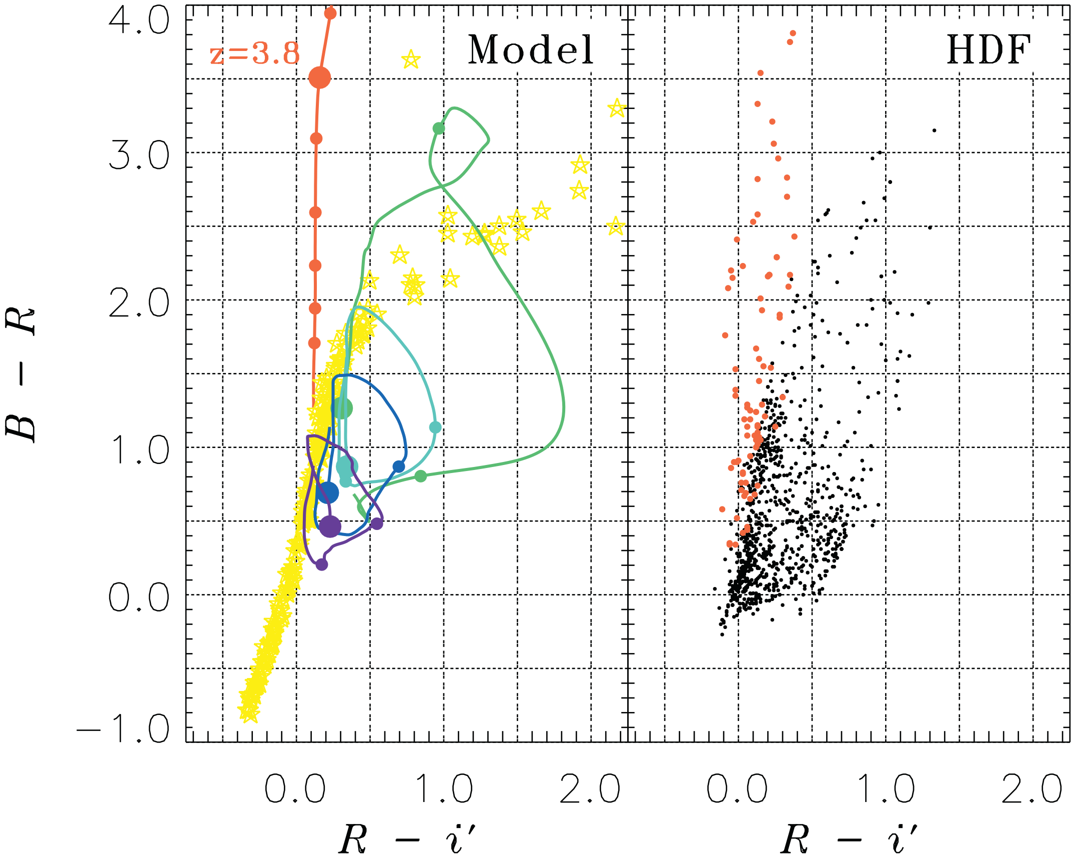

FIG. 4.—*Left*: $B - R$ vs. $R - i'$ color-color diagram displaying the colors of model galaxies and stars. The red line shows the track of a typical spectrum of star-forming galaxies from $z = 3$ to 4. The typical spectrum is produced by the GISSEL00 (Bruzual & Charlot 2003) population synthesis model with the same parameters as for the average $z \simeq 3$ galaxy (Papovich et al. 2001): a Salpeter IMF, $Z = 0.2\ Z_{\odot}$, and at 70 Myr after the initial star formation with the Calzetti et al. (2000) dust attenuation of $E(B - V) = 0.16$. Filled circles on the red line indicate the redshift from $z = 3.3$ to 3.9 with an interval of $\Delta z = 0.1$. Typical spectra of elliptical, Sbc, Scd, and irregular galaxies taken from Coleman et al. (1980) are redshifted from $z = 0$ to 3, shown by green, cyan, blue, and violet lines, respectively. Each line is marked by filled circles at $z = 0$, 1, and 2. Yellow stars show 175 Galactic stars given by Gunn & Stryker (1983). *Right*: $B - R$ vs. $R - i'$ color-color diagram displaying the colors of 1048 HDF-N photo-z galaxies obtained by convolution of their best-fit SEDs (Furusawa et al. 2000) with the filter transmissions of the Suprime-Cam. The black and red dots indicate galaxies whose photo-z values are $0 < z \leq 3$ and $z > 3$, respectively.

LBGs with a reasonably high completeness and with a low contamination from interlopers. Since the number of spectroscopically confirmed objects is very small (especially for high-z galaxies), we determine the selection criteria of the LBGs by simulations.

We use the best-fit SEDs of objects in the HDF-N photo-z catalog given by Furusawa et al. (2000). The HDF-N catalog is an appropriate catalog to be compared with our data, since it contains a number of galaxies at $z = 4-6$ calibrated with spectroscopic identifications. Another advantage of the HDF-N catalog is that it has not only blue (in UV continuum) galaxies but also red (in UV continuum) galaxies, which usually escape from Lyman break selection criteria. We already show in Figures 4–6 the colors of the 1048 HDF-N galaxies, which are calculated by convolving the best-fit SEDs with the response functions of the Suprime-Cam filters. Since the colors of these HDF-N galaxies are calculated from the best-fit SEDs, they are free from random photometric noise. The colors of objects in our catalogs, on the other hand, include random errors whose amplitudes are dependent on apparent magnitudes and local sky fluctuations. So as to evaluate these random errors, we generate artificial galaxies that mimic the HDF-N galaxies and distribute them randomly on our original images after adding Poisson noise according to their original brightness. Then, we detect these simulated objects and measure their brightness in the same manner as for our photometric catalogs (§ 2.2.2). We iterate this process 100 times and derive probability maps of the detected objects in two-color diagrams. We define low-z interlopers as galaxies whose redshifts are lower than $z = 3$ in the original photo-z catalog. In Figures 8–10 we show the probability maps of the low-z interlopers, i.e., the probability maps of contamination, thus obtained. To derive probability maps of high-z galaxies, we carry out additional simulations, since the number of high-z galaxies in the Furusawa et al. (2000) catalog is not large (52 galaxies at $z > 4$). Here, high-z galaxies are defined as galaxies whose redshifts are close to the expected central redshift given by the color selection for each of the three LBG samples. Assuming that the color distribution found for the high-z galaxies in the HDF-N catalog is universal and independent of i' (and z') magnitude, we make a mock catalog of 1648 galaxies at $z \geq 2.5$ whose i'- or z'-band magnitudes are scaled from 23.0 to 27.0 mag with a 0.5 mag interval. Then we distribute these galaxies on our original images and detect them in the same manner as for the estimation of low-z interlopers. We iterate this process 100 times, and we obtain probability maps of high-z galaxies. In Figures 8–10 we show the probability maps of high-z galaxies, i.e., probability maps of completeness. We also plot the spectroscopically identified objects in Figures 8–10. The probability maps are

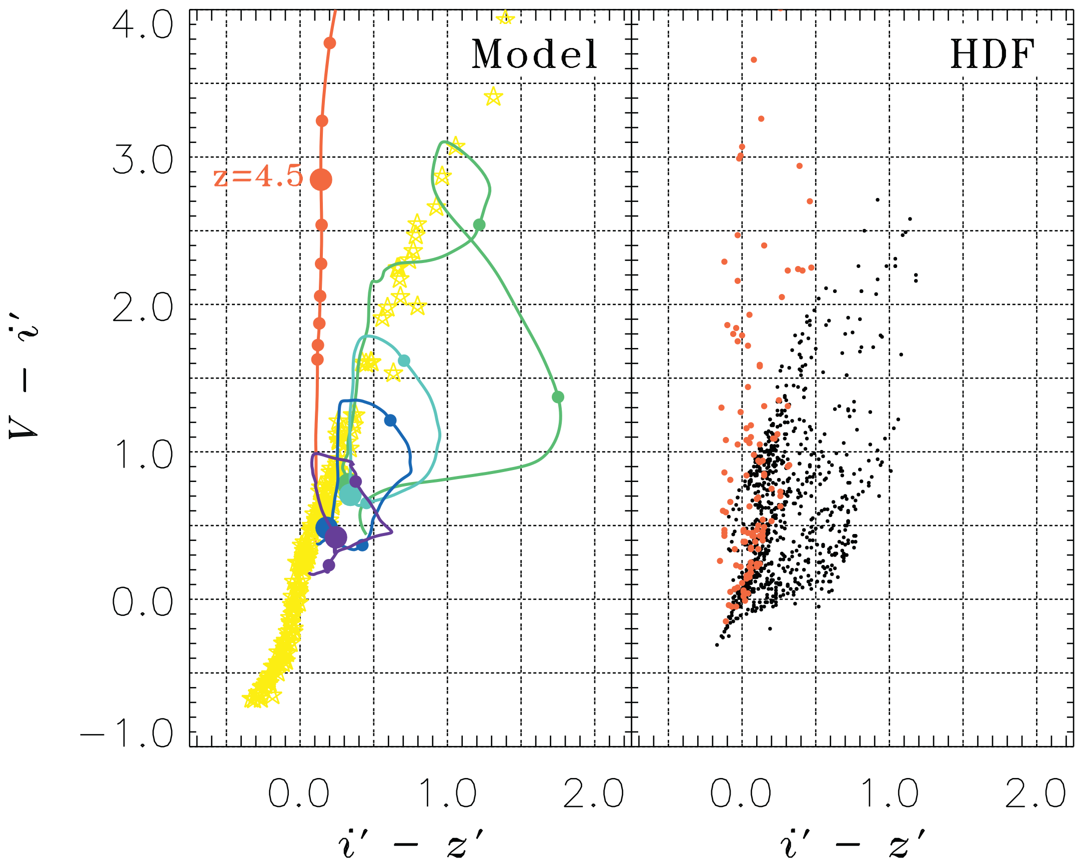

FIG. 5.—Same as Fig. 4 but for $V - i'$ vs. $i' - z'$. The filled circles on the red line in the left panel indicate the redshift from $z = 3.9$ to 4.7 with an interval of $\Delta z = 0.1$.

fairly well consistent with the color distributions of the spectroscopically identified objects.

Based on the probability maps of interlopers and high-z galaxies, we determine the selection criteria of three LBG samples that yield small contaminants and keep completeness high enough as

$$B - R > 1.2, \quad R - i' < 0.7,$$
$$B - R > 1.6(R - i') + 1.9 \text{ for } BRi\text{-LBGs}, \tag{1}$$
$$V - i' > 1.2, \quad i' - z' < 0.7,$$
$$V - i' > 1.8(i' - z') + 1.7 \text{ for } Viz\text{-LBGs}, \tag{2}$$
$$R - i' > 1.2, \quad i' - z' < 0.7,$$
$$R - i' > 1.0(i' - z') + 1.0 \text{ for } Riz\text{-LBGs}. \tag{3}$$

In Figures 8–10, green lines show these criteria. These criteria reject not only the sequences of low-z interlopers but also the tails of low-z interlopers scattered by photometric errors. Since the number density of low-z interlopers is quite large, those scattered by photometric errors become significant in number density. Figure 8 (*top left*) shows that the selection criteria of *BRi*-LBGs reject all the spectroscopically identified low-z objects and that the criteria select all the spectroscopically identified high-z galaxies at $z = 3.5$–4.5. On the other hand, Figure 9 (*top left*) shows that the selection criteria of *Viz*-LBGs reject all the spectroscopically identified low-z objects, but that the criteria miss two spectroscopically identified high-z galaxies at $z = 4.2$–5.2. These two galaxies are SDF J132416.3+274355 and SDF J132413.1+274116. Their redshifts, $z = 4.250$ and 4.270, are close to the lowest redshift ($z = 4.2$) that satisfies the criteria. This result is consistent with our simulations, which show that the criteria select just ~20% of $z \simeq 4.3$ galaxies (see Fig. 12; details are discussed later in this section). In Figure 10 (*top left*), the criteria of *Riz*-LBGs reject all the spectroscopically identified low-z interlopers, but the galaxy at $z = 4.865$ is marginally missed. Similarly, our simulations show that the criteria select about half of the galaxies at $z = 4.9$ (see Fig. 12). In summary, we can estimate well the completeness of high-z galaxies as a function of redshift from our simulations.

Figure 9 (*top right*) shows that the *Viz*-LBG sample of the SXDF contains a large number of contaminants. This is because the S/N of the SXDF V-band data is worse than that of the SDF V-band data. In order to select *Viz*-LBGs in the SXDF with a smaller number of contaminants, we define the *Viz*-LBG selection for the SXDF data as

$$V - i' > 1.2, \quad i' - z' < 0.7, \quad V - i' > 1.8(i' - z') + 2.3. \tag{4}$$

Since these criteria are quite tight, the completeness of the *Viz*-LBG sample is very low (see Fig. 12).

We apply these selection criteria to our photometric catalogs. We use i'-detection catalogs for *BRi*-LBGs and z'-detection catalogs for *Viz*-LBGs and *Riz*-LBGs. We find 1438 (732), 246 (34), and 68 (38) objects for *BRi*-LBGs, *Viz*-LBGs, and *Riz*-LBGs in the SDF (SXDF). Thus, we obtain LBG samples composed of 2556 ($\simeq$2600) LBGs in total, which are the largest LBG samples at $z = 4-5$ to date. We refer to these LBG samples as the photometric samples of LBGs. Table 3 summarizes the photometric samples.

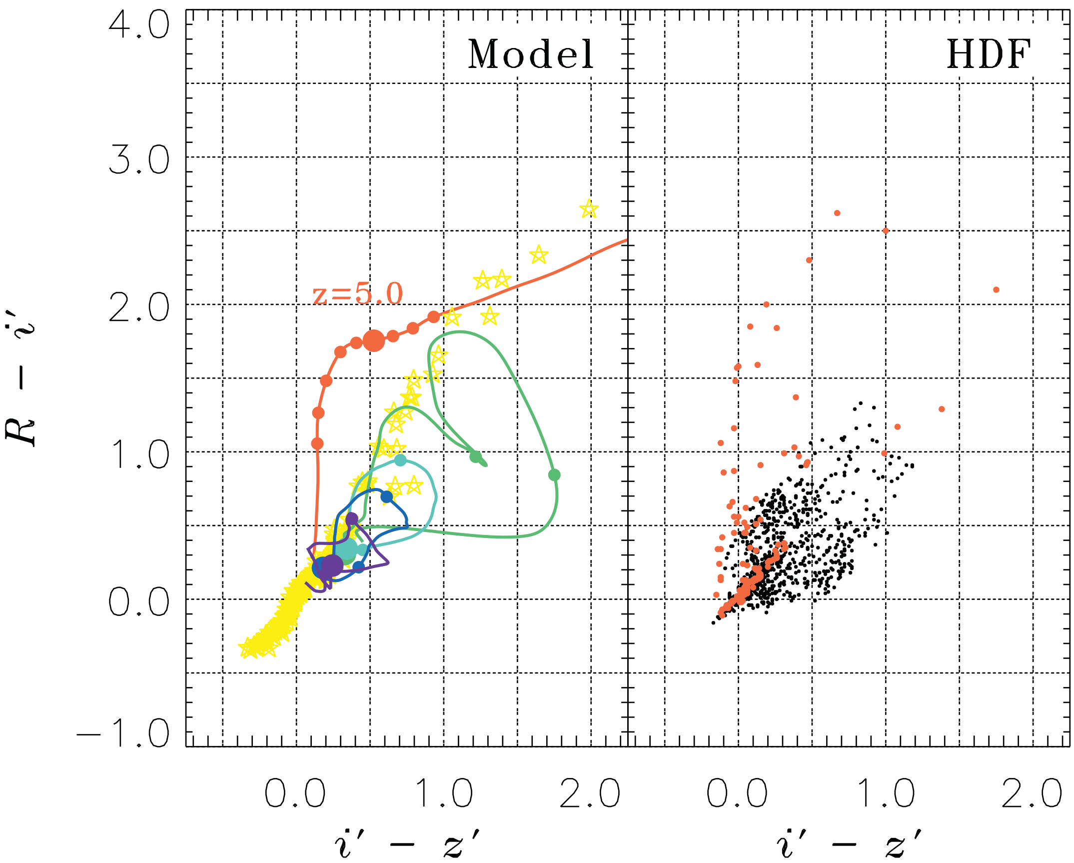

FIG. 6.—Same as Fig. 4 but for $R - i'$ vs. $i' - z'$. The filled circles on the red line in the left panel indicate the redshift from $z = 4.5$ to 5.3 with an interval of $\Delta z = 0.1$.

We show the number counts of LBGs in our samples in Figure 11, together with those obtained by Steidel et al. (1999) and Iwata et al. (2003). We find that the number counts of our LBGs are fairly comparable to those of Steidel et al. (1999), who selected LBGs at $z = 4.1 \pm 0.5$ by a two-color diagram of $Gn - R$ versus $R - I$. On the other hand, there is a large discrepancy between our counts (at bright magnitudes) and those of Iwata et al. (2003), who selected LBGs at $z = 5.0 \pm 0.5$ by a two-color diagram of $V - I_c$ versus $I_c - z'$. The reason for this discrepancy is not clear to us. The boundary of selection criteria of Iwata et al. (2003) is very close to the colors of elliptical galaxies at $z \simeq 0.5$–1.0; the separation between the boundary and the colors of foreground galaxies is only about 0.05 mag in $I_c - z'$. In reality, the two-color diagram of Iwata et al. (2003) shows that their criteria select a number of objects from the outskirts of low-z objects' color sequence in the brightest magnitude range ($I_c < 23.5$; Fig. 2*d* of Iwata et al. 2003). On the other hand, our selection criteria have a margin between LBGs and foreground objects of at least 0.2 mag. Photometric errors and small offsets in photometric zero points would easily introduce errors of 0.05 mag. Therefore, we infer that the LBG sample of Iwata et al suffers from bright foreground galaxies, which strongly affect the bright end of number counts for LBGs.

3.2. *Completeness and Contamination of the Samples*

We use the results of the simulations described in § 3.1 in order to estimate the redshift distribution, completeness, and contamination of the LBG samples. Simulated galaxies are sorted into redshift and magnitude bins with bin sizes of $\Delta z = 0.2$ and $\Delta m = 0.5$, respectively. We count the number of output high-z galaxies, $N^{\rm out}_{\text{high-}z}(m, z)$, and the number of input high-z galaxies, $N^{\rm in}_{\text{high-}z}(m, z)$, in each of the redshift and magnitude bins. We define the completeness as a function of redshift for our LBG sample as

$$C(m, z) = \begin{cases} \dfrac{N^{\rm out}_{\text{high-}z}(m, z)}{N^{\rm in}_{\text{high-}z}(m, z)}, & z \geq z_0, \\ 0, & z < z_0, \end{cases} \tag{5}$$

where z_0 is the boundary redshift between low-z interlopers and LBGs. We adopt $z_0 = 3$ in our analysis. We plot $C(m, z)$ of each LBG sample in Figure 12. The contamination of the sample is similarly defined as the ratio of the number of low-z ($z < z_0$) interlopers to the number of all the objects satisfying the selection criteria. For contamination estimation, we use the total number of contaminants lying between $z = 0$ and z_0 in each magnitude bin, because we do not need the number of contaminants as a function of redshift. Figure 13 shows the total number of contaminants and the number of selected objects as a function of magnitude. We define the contamination for a given magnitude bin as

$$f_c(m) = \frac{\int_0^{z_0} A N^{\rm out}_{\rm cont}(m, z)\, dz}{N(m)}, \tag{6}$$

where $N(m)$ and $N^{\rm out}_{\rm cont}(m)$ are, respectively, the number of objects satisfying the criteria and the number of selected interlopers in the magnitude bin, and A is a scaling factor to

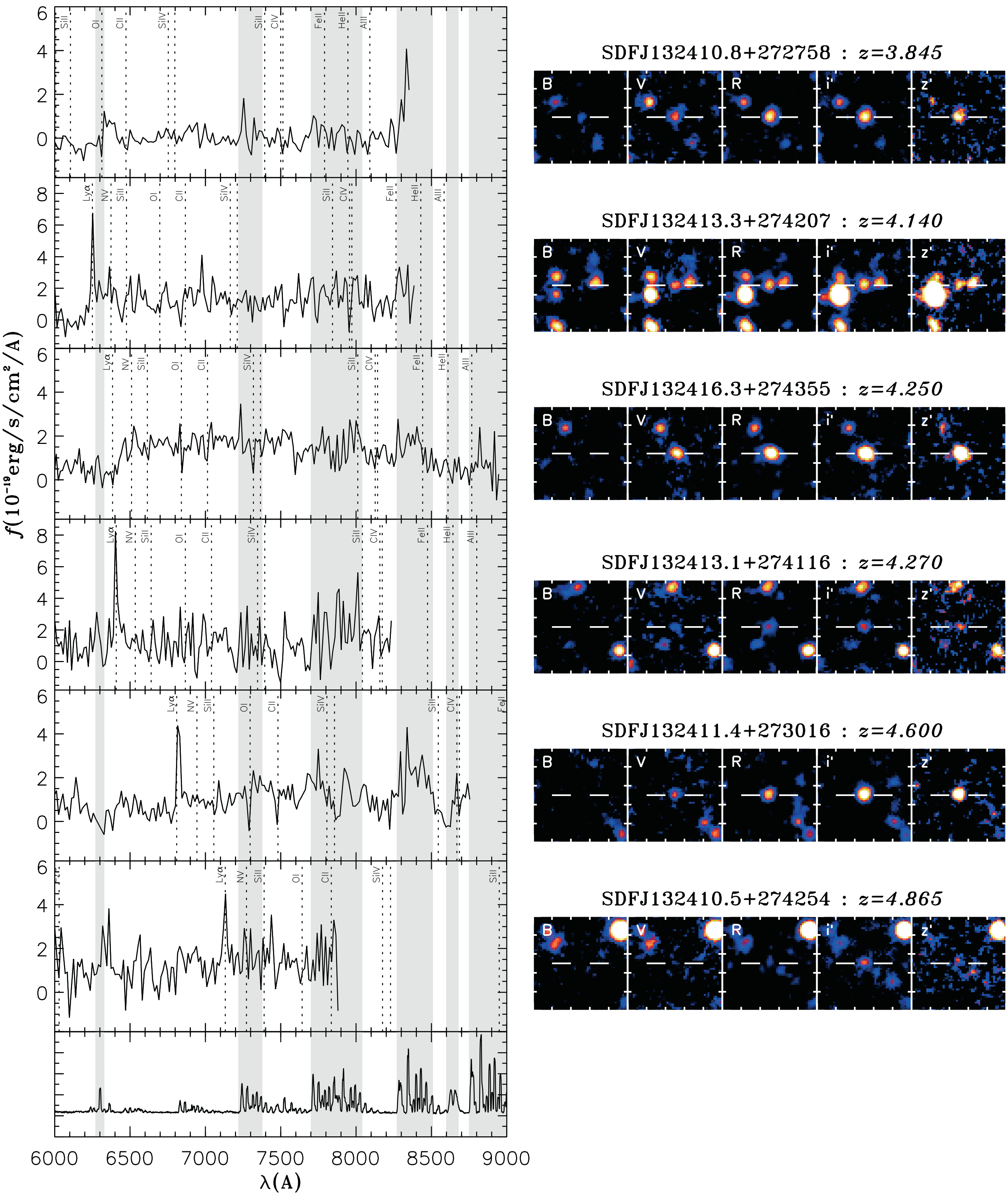

FIG. 7.—Spectra (*left panels*) and snapshots (*right panels*; *B*, *V*, *R*, *i'*, and *z'* from left to right) of six LBGs found in the SDF. Object names, coordinates, and magnitudes are listed in Table 2. The bottom left panel shows a relative night-sky spectrum. In the left panels, shaded regions correspond to the wavelength ranges in which we cannot measure spectra because of bright sky emission. In the right panels, LBGs are located in the center of each box. The box size is $10'' \times 10''$, and the tick marks on a side indicate $2''$.

TABLE 2
LBGs with Spectroscopic Redshifts

Object Name	R.A. (J2000.0)	Decl. (J2000.0)	z	B	V	R	i'	z'
SDF J132410.8+272758	13 24 10.8	+27 27 58	3.845	27.79	26.21	25.09	25.00	24.97
SDF J132413.3+274207	13 24 13.3	+27 42 07	4.140	27.84	26.10	25.32	25.16	25.17
SDF J132416.3+274355	13 24 16.3	+27 43 55	4.250	>29.0	25.54	24.54	24.09	24.02
SDF J132413.1+274116	13 24 13.1	+27 41 16	4.270	>29.0	27.32	26.08	26.10	25.91
SDF J132411.4+273016	13 24 11.4	+27 30 16	4.600	>29.0	26.61	25.40	24.66	24.51
SDF J132410.5+274254	13 24 10.5	+27 42 54	4.865	>29.0	>28.5	27.21	25.96	25.98

Notes.—Units of right ascension are hours, minutes, and seconds, and units of declination are degrees, arcminutes, and arcseconds. Magnitudes are $2''\phi$ aperture magnitudes.

account for the difference in the area between HDF-N (i.e., 4 arcmin^2) and the observed area (i.e., $\sim$600 arcmin^2).

3.3. *Galaxies Escaping from our LBG Selections*

We examine the fraction of high-z galaxies escaping from our LBG selections. There are two sources by which we miss high-z galaxies. One is photometric error, and the other is the sample bias due to the tight selection criteria of LBGs, which require ideal features for identification, i.e., a clear Lyman break and flat-UV continuum. In the following sections we investigate the statistical features of our LBG samples. Since the photometric errors are random errors, correct statistical results are obtained using the contamination and completeness given in § 3.2. On the other hand, the sample bias systematically changes the statistical results, in spite of applying the corrections. Thus, it is important to know how large a fraction of high-z galaxies our LBG selections miss.

In order to investigate this sample bias, we use the HDF-N photo-z catalog by Furusawa et al. (2000), whose high-z galaxies are not biased as strongly as those selected from any LBG criteria, which require a clear Lyman break and flat-UV continuum for identification. Since we need to know the systematic selection bias, we use the original colors of the photo-z catalog without photometric errors. Figure 14 plots the redshift distribution of the HDF-N photo-z galaxies. Galaxies that satisfy the selection criteria (eqs. [1]–[4]) are shown by filled histograms. The second, third, and bottom panels of Figure 14 present the redshift distribution of galaxies satisfying the *BRi*-LBG, *Viz*-LBG, and *Riz*-LBG selection criteria, respectively. These three panels show that most galaxies are selected if they are located at the central redshifts of the selection windows, $z \simeq 4.0$ for *BRi*-LBGs, $z \simeq 4.7$ for *Viz*-LBGs, and $z \simeq 4.9$ for *Riz*-LBGs, while the selection completeness decreases toward the outskirts of the selection windows. These behaviors are reasonable, since galaxies are selected as LBGs if their Lyman breaks and/or Lyα breaks enter the bluest band, while Lyα breaks do not enter the reddest band in each of the three band sets. The implicit assumption here is that high-z galaxies are ideally characterized by their Lyman breaks and flat-UV continuum features. However, not all galaxies share such ideal features, and some galaxies may have a weak Lyman break or a steep (red) UV continuum. In order to estimate the fraction of galaxies escaping from our *BRi*-, *Viz*-, and *Riz*-LBG selections, we show the redshifts of all galaxies that are selected by at least one of equations (1)–(3) in Figure 14 (*top*). If we focus on galaxies located at $z = 3.9-5.1$ (47 in total), where galaxies are well selected by the combination of *BRi*-, *Viz*-, and *Riz*-LBG selections, we find that four out of the 47 escape from the combination of these selections, which is just $4/47 \simeq 10\%$ in number.

We investigate the differences between the four escaping galaxies and all the other galaxies using best-fit SEDs, which reflect stellar population (age and metallicity) and dust extinction [$E(B-V)$]. We find no significant difference but for the amplitude of dust extinction. Figure 15 shows the histogram of $E(B-V)$ of galaxies in the HDF-N photo-z catalog. It is found that galaxies with heavy dust extinction, $E(B-V) \gtrsim 0.4$, tend to be missed. This trend is reasonable, because galaxies with heavy dust extinction are red in any colors, and these galaxies with red colors are outside the LBG selection criteria.

On the other hand, Pascarelle et al. (1998) point out that about 50% of galaxies escape from their LBG selection. Their claim, however, does not conflict with ours, since their definition of escaping galaxies is different from ours. Their claim is based on a comparison between $z \simeq 4$ photo-z–selected galaxies and galaxies selected by LBG criteria based on only one two-color diagram of $B-V$ versus $V-I$. If we calculate the completeness of our *BRi*-LBG sample following their definition, we find the completeness to be 61% (36 out of 59 galaxies at $z = 3.5-4.7$), which is consistent with their value (50%). Dickinson (2000) has investigated the completeness of LBG selection with a definition similar to ours. He has compared the rest-frame UV–selected LBGs with rest-frame optical–selected photo-z galaxies and found that 80% of the photo-z galaxies satisfy at least one of his LBG selections. Thus, his results are consistent with ours.

According to the results shown above, we regard our LBG samples as "extinction-uncorrected" rest-frame UV–limited samples, missing only $\sim$10% of all galaxies (in number) brighter than given extinction-uncorrected UV magnitudes. Note that this very low missing fraction does not rule out the existence of a large population of very red galaxies whose extinction-uncorrected rest-frame UV magnitudes are much fainter than the limiting magnitudes of our samples because of heavy dust extinction. Similarly, our result is compatible with the existence of passive galaxies whose UV magnitudes are fainter than our limiting magnitudes. Indeed, recent deep near-infrared observations have revealed a substantial number of red high-z galaxies that cannot be detected by the Lyman break technique because of too faint optical magnitudes (Franx et al. 2003).

4. LUMINOSITY FUNCTIONS

4.1. *LFs of LBGs*

We derive the LFs of LBGs at $z = 4-5$ from our large samples: *BRi*-LBG, *Viz*-LBG, and *Riz*-LBG samples in the SDF and SXDF. Since we do not have redshifts for individual LBGs but only the redshift distribution functions (i.e., probability density functions) given in Figure 12, we cannot calculate the LFs by conventional methods (e.g., the V/V_{max}

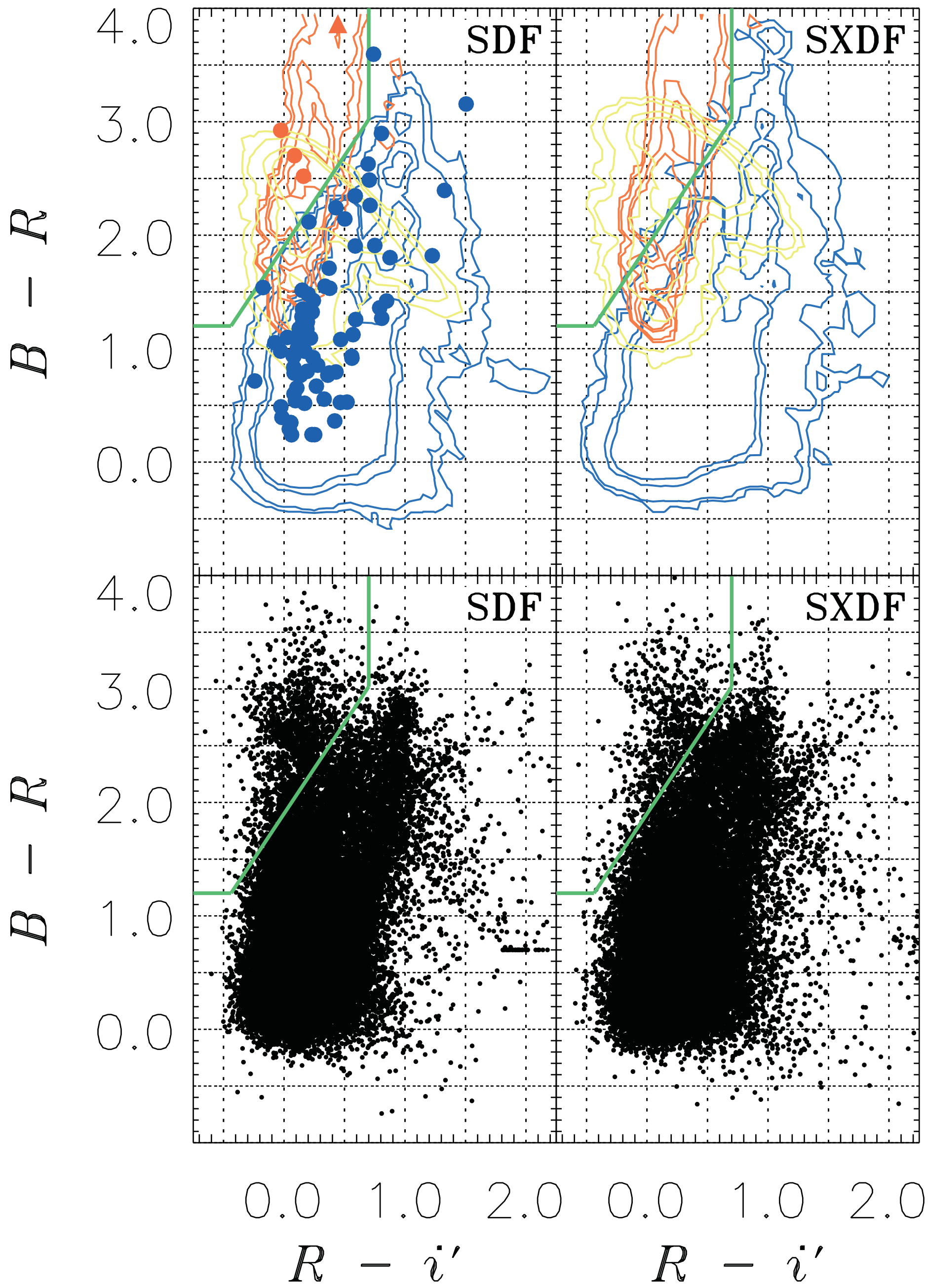

FIG. 8.—*Top panels*: $B-R$ vs. $R-i'$ color-color diagram displaying the probability maps of low-z interlopers and high-z galaxies in the SDF (*top left*) and SXDF (*top right*). The probability is estimated by Monte Carlo simulations using the best-fit SEDs of galaxies in the HDF-N photo-z catalog (Furusawa et al. 2000). Red and yellow contours show the probabilities of high-z galaxies in a bright magnitude bin ($i'=23.5-24.0$ for both fields) and a faint magnitude bin ($i'=26.0-26.5$ for SDF, $i'=25.5-26.0$ for SXDF), respectively. The four contours indicate regions that include 95%, 90%, 70%, and 50% (*from edge to center*) of the detected sources. The probability map of faint galaxies is generally wider than that of bright galaxies, since fainter galaxies have larger photometric errors. The contours for the faint galaxies do not extend to large $B-R$, because of the limited depth of the B-band data. Blue contours show the probabilities of low-z contaminants integrated over $i'<26.5$. The four contours indicate regions that include 99.5%, 99.0%, 95.0%, and 90.0% (*from edge to center*) of all the contaminants. The green line indicates the selection criteria of *BRi*-LBGs. Red and blue circles indicate 85 spectroscopically identified objects located at high redshift ($3.5<z<4.5$) and at low redshift ($0<z\leq3.5$), respectively. The red triangle denotes an object located at high redshift ($3.5<z<4.5$) but whose B-band magnitude is below the 1 σ magnitude. *Bottom panels*: $B-R$ vs. $R-i'$ colors of objects in our SDF catalog (*bottom left*: 45,923 objects with $i'<26.5$) and SXDF catalog (*bottom right*: 39,301 objects with $i'<26.0$). A dot indicates an object. If the magnitude of an object is fainter than the 1 σ magnitude (1 σ sky fluctuation), then the magnitude is replaced with the 1 σ magnitude. This replacement produces artificial sequences in the two-color diagram around $(R-i',\ B-R)=(1.5,\ 1.0)$ and (2.0, 0.7) for the SDF and $(R-i',\ B-R)=(1.5,\ 1.4)$ and (2.1, 0.7). for the SXDF. The green line indicates the selection criteria of *BRi*-LBGs.

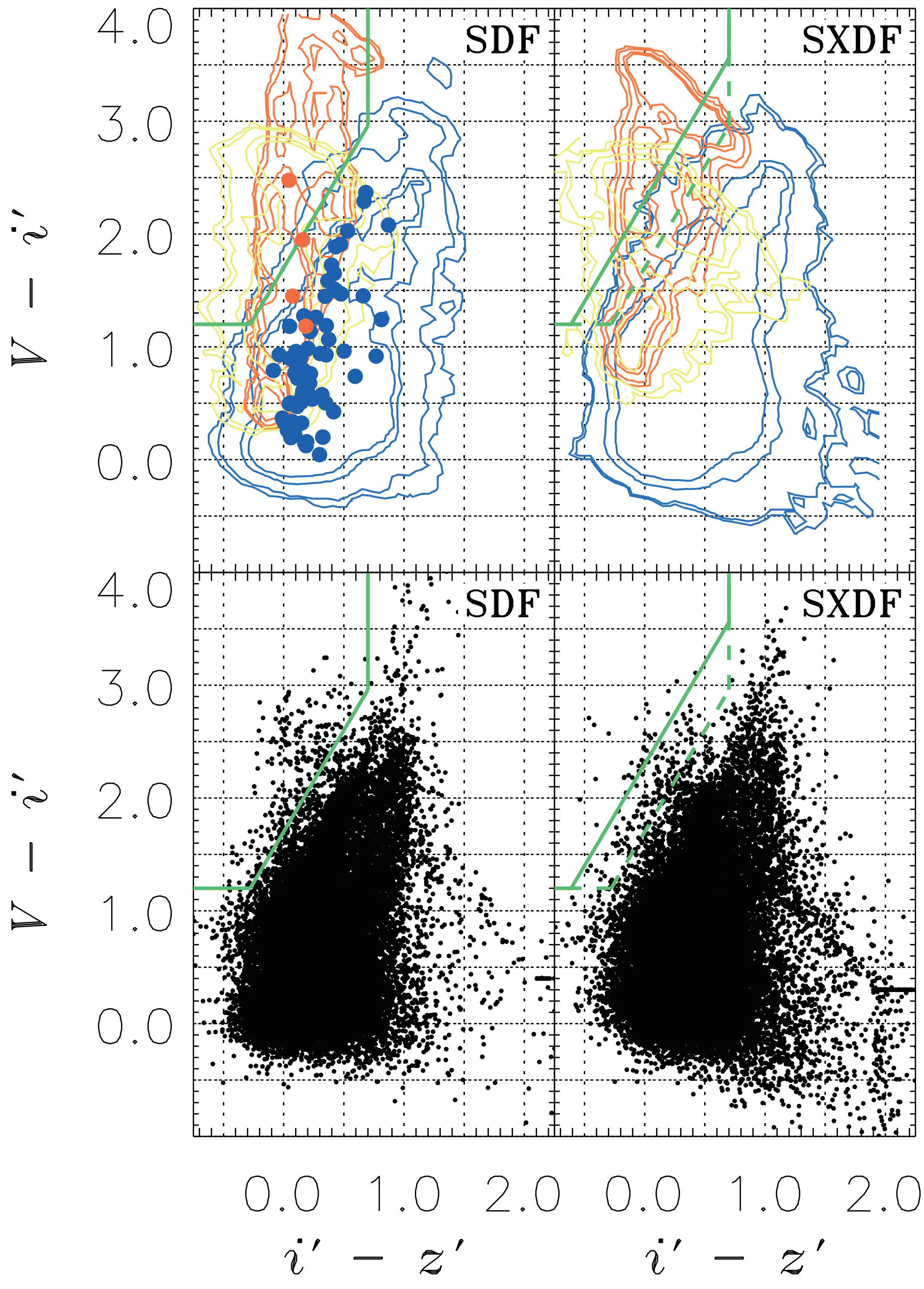

FIG. 9.—*Top panels*: Same as the top panels of Fig. 8 but for $V - i'$ vs. $i' - z'$. Red and yellow contours show the probabilities of high-z galaxies in a bright magnitude bin ($z' = 24.0 - 24.5$ for both fields) and a faint magnitude bin ($z' = 25.5 - 26.0$ for SDF, $z' = 25.0 - 25.5$ for SXDF), respectively. Green solid lines indicate the selection criteria of *Viz*-LBGs for the SDF data. The green dotted line in the right panel shows the criteria of *Viz*-LBGs for the SXDF data (eq. [4]). Red and blue circles indicate 85 spectroscopically identified objects located at high redshift ($4.2 < z < 5.2$) and at low redshift ($0 < z \leq 4.2$), respectively. The two red points far below the selection criteria denote galaxies at $z = 4.250$ and 4.270. Since the selection criteria of *Viz*-LBGs have a completeness of just $\sim$20% for these redshifts, it is consistent that the colors of these two galaxies are well separated from the selection criteria. These two galaxies are selected by the criteria for *BRi*-LBGs. *Bottom panels*: Same as the bottom panels of Fig. 8 but for $V - i'$ vs. $i' - z'$ colors of objects in our SDF catalog (*bottom left*: 37,486 objects with $z' < 26.0$) and SXDF catalog (*bottom right*: 34,024 objects with $z' < 25.5$). A dot indicates an object. If the magnitude of an object is fainter than the 1 σ magnitude (1 σ sky fluctuation), then the magnitude is replaced with the 1 σ magnitude. This replacement produces artificial sequences in the two-color diagram around $(i' - z',\ V - i') = (1.5,\ 1.3)$ and (2.2, 0.4) for the SDF and $(i' - z',\ V - i') = (1.5,\ 0.9)$ and (2.0, 0.3) for the SXDF. Green solid lines indicate the selection criteria of *Viz*-LBGs for the SDF data. The green dotted line in the right panel shows the criteria of *Viz*-LBGs for the SXDF data (eq. [4]).

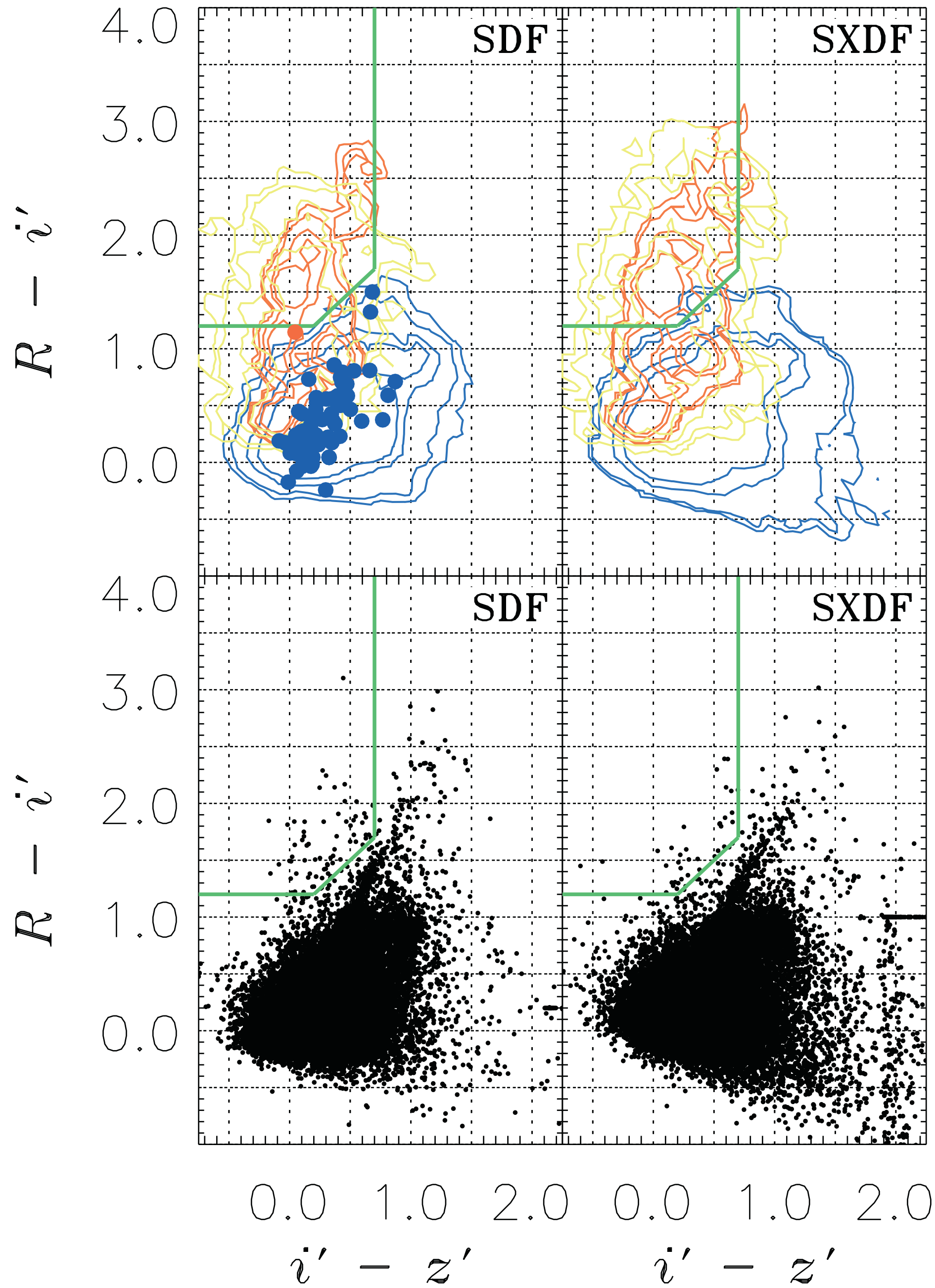

FIG. 10.—*Top panels*: Same as the top panels of Fig. 8 but for $R - i'$ vs. $i' - z'$. Red and yellow contours show the probabilities of high-z galaxies in a bright magnitude bin ($z' = 24.0-24.5$ for both fields) and a faint magnitude bin ($z' = 25.5-26.0$ for SDF, $z' = 25.0-25.5$ for SXDF), respectively. Green lines indicate the selection function of *Riz*-LBGs. Red and blue circles indicate 85 spectroscopically identified objects located at high redshift ($4.6 < z < 5.2$) and at low redshift ($0 < z \leq 4.2$), respectively. The red point denotes a galaxy at $z = 4.865$. This galaxy is not included in the *Riz*-LBG sample (probably because of its photometric errors) but is identified by the selection criteria of *Viz*-LBGs. *Bottom panels*: Same as the bottom panels of Fig. 8 but for $R - i'$ vs. $i' - z'$ colors of objects in our SDF catalog (*bottom left*: 37,486 objects with $z' < 26.0$) and SXDF catalog (*bottom right*: 34,024 objects with $z' < 25.5$). A dot indicates an object. If the magnitude of an object is fainter than the 1 σ magnitude (1 σ sky fluctuation), then the magnitude is replaced with the 1 σ magnitude. This replacement produces artificial sequences in the two-color diagram around $(i' - z',\ R - i') = (1.5,\ 1.0)$ and (2.2, 0.2) for the SDF and $(i' - z',\ R - i') = (2.0,\ 1.0)$ and (2.0, 0.0) for the SXDF. Green lines indicate the selection criteria of *Riz*-LBGs.

TABLE 3
PHOTOMETRIC SAMPLES OF GALAXIES

Field Name	Sample Name	Detection Band	Number	Magnitude Range[a]	Selection Criteria
SDF	*BRi*-LBG	i'	1438	i' = 23.5–26.5	Eq. (1)
SDF	*Viz*-LBG	z'	246	z' = 24.0–26.0	Eq. (2)
SDF	*Riz*-LBG	z'	68	z' = 24.0–26.0	Eq. (3)
SXDF	*BRi*-LBG	i'	732	i' = 23.5–26.0	Eq. (1)
SXDF	*Viz*-LBG	z'	34[b]	i' = 23.5–25.5	Eq. (4)
SXDF	*Riz*-LBG	z'	38	i' = 24.0–25.5	Eq. (3)

[a] For $2''\phi$ aperture magnitudes.
[b] *Viz*-LBGs of the SXDF are selected by eq. (4).

method). However, our LBG samples are close to volume-limited samples, since for each sample the width of the redshift distribution divided by the mean redshift of the sample is sufficiently small. Hence, to calculate the LF for a given sample, we assign the mean redshift of the sample to all galaxies in it. For each sample, using the ratio of contamination (eq. [6]), we calculate the number density, $n(m)$, of LBGs in a given magnitude bin by

$$n(m) = \frac{N(m)[1 - f_c(m)]}{\int_{z_0}^{\infty}(dV/dz)C(m,\ z)\,dz}, \qquad (7)$$

where $N(m)$ is the number of objects satisfying the criteria in a given magnitude bin, dV/dz is the differential volume, and z_0 (=3) is the boundary redshift between low-z interlopers and LBGs. Figure 16 plots the LFs of LBGs at $z = 4.0 \pm 0.5$ (*BRi*-LBGs), $z = 4.7 \pm 0.5$ (*Viz*-LBGs), and $z = 4.9 \pm 0.3$ (*Riz*-LBGs), where the abscissa is the absolute magnitude at the rest-frame 1700 Å. The absolute magnitude at 1700 Å is estimated from the i' magnitude for *BRi*-LBGs, and from the z' magnitude for *Viz*-LBGs and *Riz*-LBGs as follows: Most of the LBGs have PSF-like (FWHM $\simeq 1''$) shapes. We find from simulations made in § 3.1 that $2''\phi$ aperture magnitudes of PSF objects are fainter than the total magnitudes by 0.2 mag for FWHM $\simeq 1''$, on average. Thus, we calculate the total magnitude from the $2''\phi$ aperture magnitude, adding an aperture correction of -0.2 mag. Then, we add a constant k-correction

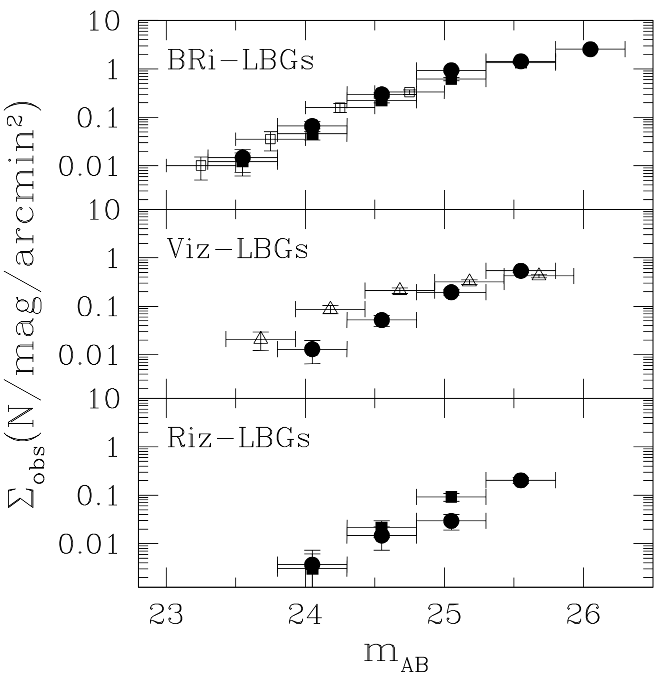

FIG. 11.—Number counts of the LBGs selected in the SDF and SXDF. *BRi*-LBGs, *Viz*-LBGs, and *Riz*-LBGs are shown separately. The magnitude, m_{AB}, is the i'-band magnitude for *BRi*-LBGs and the z'-band magnitude for *Viz*-LBGs and *Riz*-LBGs. The circles and filled squares show data from the SDF and SXDF, respectively. Since the selection criteria for *Viz*-LBGs are different between the SDF and the SXDF, we do not plot data for *Viz*-LBGs in the SXDF to avoid confusion. Open squares (*top*) and triangles (*middle*) indicate the measurements for LBGs at $z \simeq 4$ and 5 obtained by Steidel et al. (1999) and Iwata et al. (2003), respectively. The number counts of our LBGs at $z \sim 4$ agree well with those of Steidel et al., while for *Viz*-LBGs a large discrepancy is seen at bright magnitudes between our measurements and those of Iwata et al. See the text for more details.

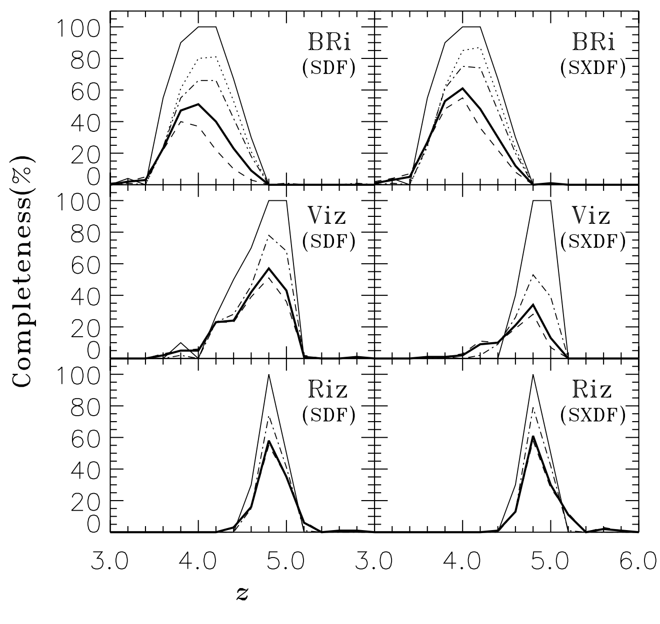

FIG. 12.—Completeness as a function of redshift for our LBG samples. In the panels for the *BRi*-LBGs, thin solid, dotted, dot-dashed, and dashed lines denote the completeness for *BRi*-LBGs with $i' = -\infty$, 24.25, 25.25, and 26.25 ($i' = -\infty$, 23.75, 24.75, and 25.75) in the SDF (SXDF). In the panels for the *Viz*-LBGs and *Riz*-LBGs, thin solid, dot-dashed, and dashed lines denote the completeness for *Viz*-LBGs and *Riz*-LBGs with $z' = -\infty$, 24.75, and 25.75 ($z' = -\infty$, 24.25, and 25.25) in the SDF (SXDF). The thick solid lines plotted in all panels show the number-weighted completeness, which is calculated by averaging the magnitude-dependent completeness weighted by the number of selected LBGs in each magnitude bin ($\Delta m = 0.5$). Since tighter selection criteria (eq. [4]) are applied to *Viz*-LBGs in the SXDF, their selection window is narrower than that of *Viz*-LBGs in the SDF. Note that the peak sensitivity of the *Riz*-LBG selection is at a slightly lower redshift than that of the *Viz*-LBG selection. This is because we have set a tighter selection boundary near the high-z end ($z \simeq 5$) in the *Riz*-LBG selection than in the *Viz*-LBG selection to avoid interlopers, since galaxies near $z = 5$ have colors in $R - i'$ and $i' - z'$ close to low-z interlopers (Figs. 6 and 10).

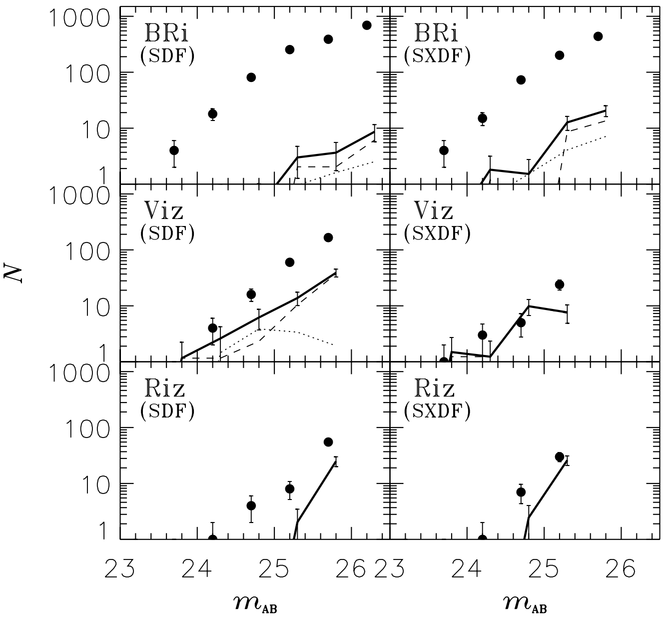

FIG. 13.—Number of contaminants and selected LBGs as a function of magnitude. Solid lines with error bars show the number of all contaminants ($N^{\rm out}_{\rm cont}$ in eq. [6]). Dashed and dotted lines indicate the number of low-z galaxies ($N^{\rm out}_{{\rm low}\text{-}z}$) and Galactic stars ($N^{\rm out}_{\rm star}$), where $N^{\rm out}_{\rm cont}$ is the sum of these two contaminants. The majority of the contaminants are low-z galaxies for *Viz*-LBGs in the SXDF and *Riz*-LBGs in the SDF and SXDF. Circles show the numbers of objects selected by respective LBG criteria. Magnitude, $m_{\rm AB}$, is i' for the *BRi*-LBGs and z' for the *Viz*-LBGs and *Riz*-LBGs.

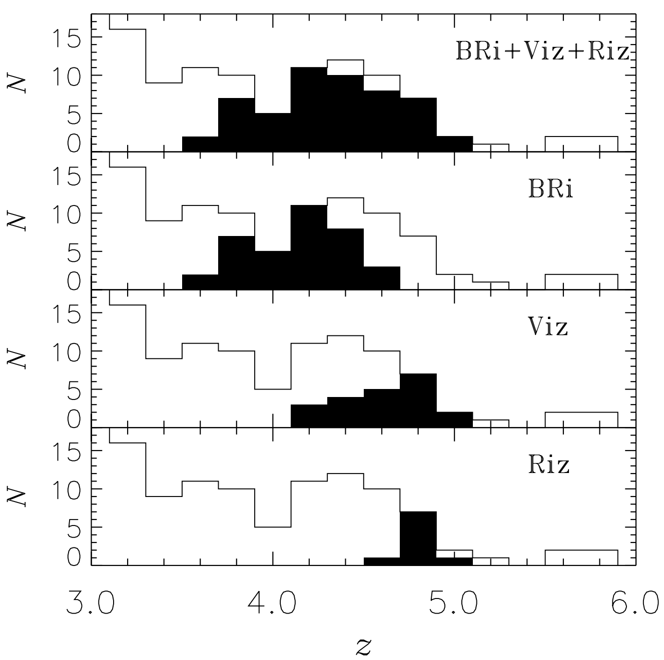

FIG. 14.—Redshift distribution of galaxies in the Furusawa et al. (2000) HDF-N photo-z catalog. In all panels, open histograms are for all galaxies in the catalog. Filled histograms are for galaxies that satisfy at least one of our *BRi*-, *Viz*-, or *Riz*-LBG selections (*first panel*), the *BRi*-LBG selection (*second panel*), the *Viz*-LBG selection (*third panel*), and the *Riz*-LBG selection (*fourth panel*). The first panel indicates that at $z = 3.9-5.1$, four out of the 47 galaxies escape from our LBG selections.

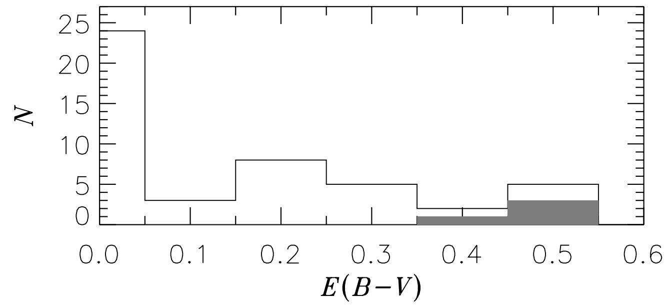

FIG. 15.—Histogram of $E(B-V)$ of galaxies in the Furusawa et al. (2000) HDF-N photo-z catalog. The open histogram shows all galaxies in the catalog. The shaded histogram shows the distribution of the four galaxies that are not selected by any of the LBG selection criteria. The four galaxies have a dust extinction larger than $E(B-V) = 0.35$.

factor, -0.03 for *BRi*-LBGs and -0.01 for *Viz*-LBGs and *Riz*-LBGs, to the total magnitude. These values correspond to the median colors of $m_{1700}(z = 4.0) - i'$, $m_{1700}(z = 4.7) - z'$, and $m_{1700}(z = 4.9) - z'$, respectively, for the HDF-N photo-z galaxies at $z = 3.5$–4.5, 4.2–5.2, and 4.6–5.2 (Furusawa et al. 2000), where $m_{1700}(z = 4.0)$, $m_{1700}(z = 4.7)$, and $m_{1700}(z = 4.9)$ are the magnitudes at the rest-frame 1700 Å for galaxies at $z = 4.0$, 4.7, and 4.9, respectively.

We find in Figure 16 that the LFs obtained from the SDF and the SXDF data show an excellent consistency. Thus, we

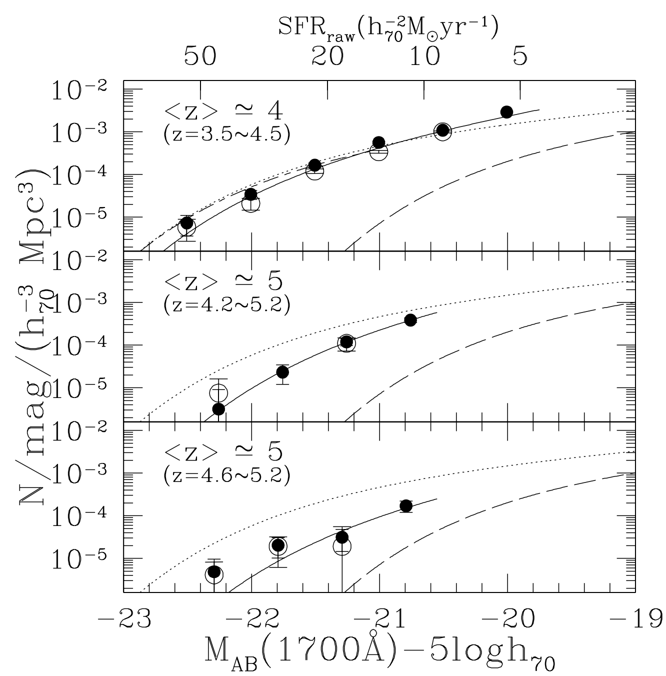

FIG. 16.—LFs of *BRi*- (*top*), *Viz*- (*middle*), and *Riz*-LBGs (*bottom*) at $z = 4-5$. In each panel, filled and open circles show the LFs derived from the SDF and SXDF data, respectively. Solid lines show the best-fit Schechter function, whose parameters are shown in Table 4 (see text). Dashed lines denote the LF of UV-selected galaxies in the local universe (Sullivan et al. 2000), while dotted lines show the LF of LBGs at $z \simeq 3$ derived by Steidel et al. (1999). In the top panel, the best-fit Schechter function of LBGs at $z = 4$ (Steidel et al. 1999) is shown by the short-dashed–long-dashed line down to approximately -21 mag. Steidel et al. (1999) measured the LF down to approximately -21 mag with their wide-field LBG survey and fitted the Schechter function with a fixed slope ($\alpha = -1.6$). The upper abscissa axis, $\rm SFR_{raw}$, indicates the SFR without extinction correction, which is converted from M_{1700} using eq. (12). The true (extinction-corrected) SFR is about a factor of 4 larger than the raw rate. See the text for details.

TABLE 4
Summary of the LFs

Sample Name	z	ϕ^* (h_{70}^3 Mpc^{-3})	M^*_{1700} (mag)	α	$n^{\rm obs\,a}$ (h_{70}^3 Mpc^{-3})	$\rho_{\rm UV}^{\rm obs\,a}$ (ergs s^{-1} Hz^{-1})	$\rho_{\rm UV}^{\rm total\,b}$ (ergs s^{-1} Hz^{-1})
BRi-LBG	$4.0^{+0.5}_{-0.5}$	$1.2 \pm 0.2 \times 10^{-3}$	-21.0 ± 0.1	-2.2 ± 0.2	$2.0 \pm 0.3 \times 10^{-3}$	$1.2 \pm 0.2 \times 10^{26}$	$2.9 \pm 0.4 \times 10^{26}$
Viz-LBG............	$4.7^{+0.5}_{-0.5}$	$1.4 \pm 0.8 \times 10^{-3}$	-20.7 ± 0.2	-2.2 (fix)	$2.8 \pm 1.7 \times 10^{-4}$	$2.7 \pm 1.8 \times 10^{25}$	$2.4 \pm 1.4 \times 10^{26}$
Riz-LBG	$4.9^{+0.3}_{-0.3}$	$\simeq 6.4 \times 10^{-4}$	-20.6 (fix)	-2.2 (fix)	$\simeq 1.1 \times 10^{-4}$	$\simeq 1.1 \times 10^{25}$	$\simeq 1.1 \times 10^{26}$
BRi-LBG	$4.0^{+0.5}_{-0.5}$	$2.8 \pm 0.2 \times 10^{-3}$	-20.6 ± 0.1	-1.6 (fix)	$1.8 \pm 0.1 \times 10^{-3}$	$1.1 \pm 0.1 \times 10^{26}$	$2.4 \pm 0.2 \times 10^{26}$ ($4.3 \pm 0.3 \times 10^{26}$)
Viz-LBG............	$4.7^{+0.5}_{-0.5}$	$2.4 \pm 1.0 \times 10^{-3}$	-20.3 ± 0.2	-1.6 (fix)	$2.7 \pm 1.2 \times 10^{-4}$	$2.7 \pm 1.3 \times 10^{25}$	$1.6 \pm 0.7 \times 10^{26}$ ($2.9 \pm 1.2 \times 10^{26}$)
Riz-LBG	$4.9^{+0.3}_{-0.3}$	$\simeq 1.0 \times 10^{-3}$	-20.3 (fix)	-1.6 (fix)	$\simeq 1.1 \times 10^{-4}$	$\simeq 1.0 \times 10^{25}$	$\simeq 7.0 \times 10^{25}$ ($\simeq 1.2 \times 10^{26}$)
LAE[c]	$4.86^{+0.03}_{-0.03}$	1.9×10^{-3}	-20.0	-1.6 (fix)	1.5×10^{-3}	5.0×10^{25}	9.6×10^{25}

Notes.—We refer to the values of *BRi*-LBGs and *Viz*-LBGs as those of $z = 4$ and $z = 5$ LBGs, since the values for *Riz*-LBGs are quite uncertain. In §§ 6.1 and 6.2 we use values obtained for $\alpha = -1.6$.

[a] Number density ($n^{\rm obs}$) and luminosity density ($\rho_{\rm UV}^{\rm obs}$) down to the observed limiting magnitudes; $M_{1700} = -19.8$ ($i'_{\rm ap} = 26.5$) for *BRi*-LBGs, $M_{1700} = -20.5$ ($z'_{\rm ap} = 26.0$) for *Viz*-LBGs, $M_{1700} = -20.5$ ($z'_{\rm ap} = 26.0$) for *Riz*-LBGs, and $M_{1700} = -19.03$ ($i'_{\rm ap} = 27.5$) for LAEs, where $i'_{\rm ap}$ and $z'_{\rm ap}$ are the $2''\phi$ aperture magnitudes in i' and z', respectively, and M_{1700} is the rest-frame 1700 Å absolute magnitude after aperture correction and k-correction (see text for details).

[b] Total luminosity density ($\rho_{\rm UV}^{\rm total}$) calculated by integrating the LF down to $L = 0.1L^*$, assuming $\alpha = -2.2$ or -1.6. Values in parentheses are upper limits, which are calculated by integrating the LF down to $L = 0$ assuming $\alpha = -1.6$.

[c] LAEs at $z = 4.86 \pm 0.03$ obtained by Paper II. We use the best-fit UV LF given in Paper II to calculate the UV-luminosity density.

believe that our results do not suffer from field variance. Then we fit the Schechter function (Schechter 1976),

$$\psi(M)\,dM = C\phi^* \exp\{-C(\alpha+1)(M-M^*) - \exp[-C(M-M^*)]\}\,dM, \quad (8)$$

to the LFs, where $C \equiv 0.4\ln(10)$, α is the power-law slope, ϕ^* is the normalization factor, which has a dimension of the number density of galaxies, L^* is the characteristic luminosity, and M^* is the characteristic absolute magnitude. First, we fit the Schechter function with three free parameters, ϕ^*, M^*, and α, to the data and find that these parameters cannot be constrained well except for the *BRi*-LBGs. Thus, for the *Viz*-LBG LF, we fix α and determine ϕ^* and M^* from fitting. For the *Riz*-LBG LF, we fix M^* as well as α, since even two-parameter fitting (ϕ^* and M^*) fails to give a reliable result. We adopt two values of α, -2.2 and -1.6, for the *Viz*-LBGs and *Riz*-LBGs, where $\alpha = -2.2$ is the best-fit value for our *BRi*-LBGs and $\alpha = -1.6$ is the best-fit value for $z = 3$ LBGs, obtained by Steidel et al. (1999). By taking a common α-value, we can make a fair comparison of the luminosity density extrapolated beyond the detection limits between our samples (see § 6). For the M^* of the *Riz*-LBG LF, we adopt an absolute magnitude calculated by linearly extrapolating the M^* values at $z = 4.0$ (*BRi*-LBGs) and $z = 4.7$ (*Viz*-LBGs) to $z = 4.9$. We present the best-fit parameters for the three samples in Table 4, together with, for comparison, those for LAEs at $z = 4.86$ obtained in Paper II. Since the Schechter fit for *Riz*-LBGs is quite uncertain, we refer to the results of *BRi*-LBGs and *Viz*-LBGs as the Schechter parameters of $z = 4$ and $z = 5$ LBGs, respectively, in the following discussion (§ 6), when we do not specify the sample names.

We plot the best-fit Schechter functions in Figure 16, together with those of LBGs at $z = 3$ and 4 measured by Steidel et al. (1999), and UV-selected galaxies at $z \simeq 0$ given by Sullivan et al. (2000). Figure 16 shows that the LF at $z = 4$ is not much different from that at $z = 3$. However, the number density of galaxies at faint magnitudes appears to be slightly higher at $z = 4$ than at $z = 3$, resulting in the steeper faint-end slope, $\alpha = -2.2 \pm 0.2$, for our $z = 4$ LBGs than the $\alpha = -1.6$ obtained by Steidel et al. (1999) for $z = 3$ LBGs. Hence, the slope of the LF may be steeper at $z = 4$ than at $z = 3$. Note that α for our LBGs is obtained from the *BRi*-LBG sample, whose limiting magnitude reaches only $M^* + 1$. Thus, the estimated slope of $\alpha = -2.2 \pm 0.2$ may include a large systematic error.

In Figure 16 we find that the number density of bright LBGs with $M_{1700} \sim -22$ decreases from $z = 4$ to 5. This tendency is found between *BRi*-LBGs and *Riz*-LBGs, as well as between *BRi*-LBGs and *Viz*-LBGs. Furthermore, the bright *Riz*-LBGs (i.e., LBGs at $z = 4.9 \pm 0.3$) might be less numerous than the bright *Viz*-LBGs (i.e., LBGs at $z = 4.7 \pm 0.5$), implying that the number density of bright LBGs tends to drop at higher redshift, although the data points of *Riz*-LBGs have a large uncertainty. The difference between $z = 4$ and 5 is about 1 order in number density at $M_{1700} \sim -22$. Since the luminosity at 1700 Å is approximately proportional to the SFR, the observed decrease in bright LBGs with $M_{1700} \sim -22$ probably indicates that galaxies with high star formation activity ($\sim$100 and 30 $h_{70}^{-2}\ M_\odot$ yr^{-1} with and without extinction correction; details are described in § 7) are rarer at $z = 5$.

The error bars of the LFs in Figure 16 correspond to Poisson errors, and we have not included errors arising from the contamination and completeness corrections. In order to evaluate how these corrections affect the results, we vary the color-selection criteria (eqs. [1]–[4]) by ± 0.15 mag in each color. [For example, we select *BRi*-LBGs with $B - R > 1.2 \pm 0.15$, $R - i' < 0.7 \pm 0.15$, $B - R > 1.6(R - i') + 1.9 \pm 0.15$.] We derive number counts of the selected objects and correction factors (i.e., contamination and completeness) with the varied color-selection criteria. Then LFs are calculated from the number counts and the correction factors. We find that the LFs with different criteria are consistent with the LFs plotted in Figure 16 within a factor of $\lesssim 2$ in number density and that the changes in criteria, although they give different correction factors, do not change the three tendencies, i.e., no significant change from $z = 3$ to 4, a decrease in number density at the bright magnitudes from $z = 4$ to 5, and a steep faint-end slope for $z = 4$ LBGs. Therefore, we conclude that these tendencies are real.

5. DUST EXTINCTION

5.1. *UV Slopes versus E(B − V)*

The steepness of the ultraviolet spectral slope (UV slope) of galaxies is a good measure of dust extinction, $E(B - V)$, since

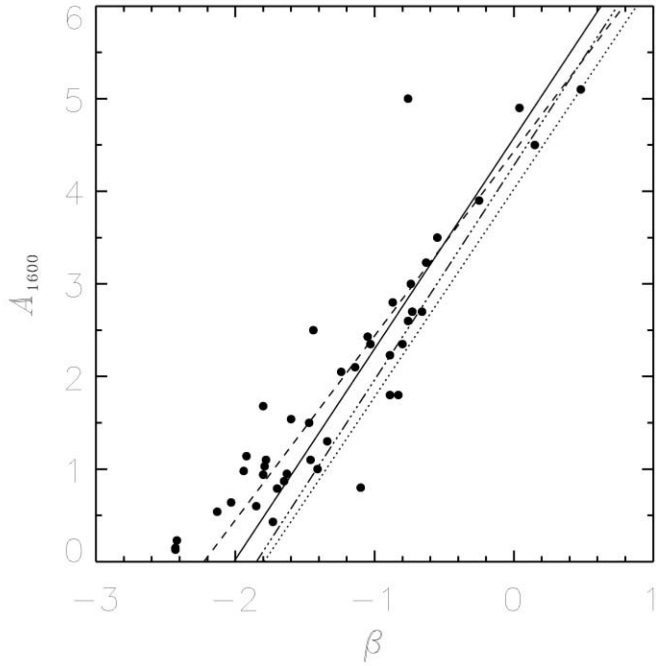

FIG. 17.—Internal absorption at 1600 Å (A_{1600}) plotted against β. The solid line shows the relation for the template spectrum (70 Myr age and 0.2 $Z_\odot$ metallicity). Filled circles indicate 43 nearby star-forming galaxies, and the dashed line shows a linear fit to the data given by Meurer et al. (1999). The dotted line is for a model spectrum that has the same age as the template spectrum (70 Myr) but a higher metallicity of 1 $Z_\odot$. The dot-dashed line is for a model spectrum that has the same metallicity as the template spectrum (0.2 $Z_\odot$) but an older age of 90 Myr.

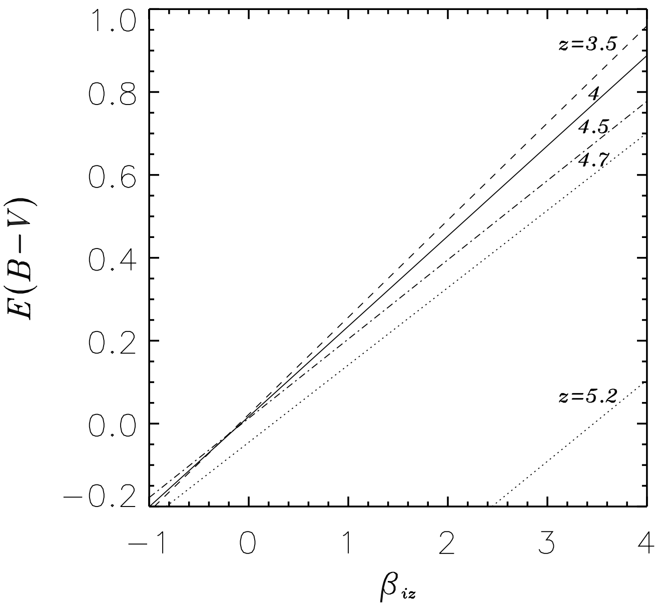

FIG. 18.—Redshift dependence of the $E(B-V)$–β_{iz} relationship calculated from the template model. The solid line is the relation for LBGs at $z = 4$, and the dashed and dot-dashed lines are for $z = 3.5$ and 4.5, respectively. The difference in the relation for LBGs at $z = 3.5-4.5$ is less than ±0.05 mag in $E(B-V)$ for LBGs with $E(B-V) \leq 0.5$. The upper and lower dotted lines are the relations of LBGs at $z = 4.7$ and 5.2, respectively.

the UV continuum is sensitive to dust extinction. Meurer et al. (1999) show that the UV slope of local star-forming galaxies has a good correlation with infrared luminosity and the dust extinction obtained from the Balmer decrement (see Calzetti 2001 for a general review). The UV slope, β, is defined as

$$f_\lambda \propto \lambda^\beta, \tag{9}$$

where f_λ is the spectrum of a galaxy over the rest-frame wavelength of ~1000 to ~3000 Å and β is the best-fit power-law index to the spectrum.

We estimate the dust extinction for our LBGs from the UV slope. We choose the $i' - z'$ color for estimating the UV slopes of *BRi*-LBGs (at $z \simeq 4$), since $R - i'$ and $R - z'$ colors are affected by Lyα emission and the trough of Lyα absorption systems, while $i' - z'$ samples the continuum at more than 1216 Å. We do not calculate UV slopes for *Viz*- or *Riz*-LBGs, since Lyα emission and the trough of Lyα absorption systems enter the i' band.

Although β is originally defined as the index of the best-fit power law (eq. [9]) in the wavelength range of ~1000 to ~3000 Å, the definition of the wavelength range varies among authors, e.g., 1100–3000 and 1200–1800 Å (see Calzetti 2001). In order to measure the UV slope of LBGs at $z = 4$ from the $i' - z'$ color, we define β_{iz} as

$$\beta_{iz} \equiv -\frac{i' - z'}{2.5 \log\left[\lambda_c(i')/\lambda_c(z')\right]} = 5.42(i' - z'), \tag{10}$$

where $\lambda_c(i')$ and $\lambda_c(z')$ are the central wavelengths of the i' and z' bands.

We use the latest version of the Bruzual A. & Charlot (1993) stellar population synthesis model (GISSEL00; Bruzual & Charlot 2003) convolved with the extinction curve of Calzetti et al. (2000).[15] We generate a template spectrum whose model parameters have the average values observed for LBGs at $z = 3$, which are given in Papovich et al. (2001), that is, a 70 Myr age, a 0.2 $Z_\odot$ metallicity, and a Salpeter IMF. Figure 17 compares the extinction-β relation of the template spectrum with the measurements for 43 nearby galaxies (Meurer et al. 1999). The fitting is made over 1250–2600 Å for both the template spectrum and nearby galaxies.

The extinction-β relation from our template spectrum (*solid line*) shows fairly good agreement with the data points of the nearby galaxies (*circles*) and with the best-fit line (*dashed line*) derived by Meurer et al. (1999). The template, the typical LBG spectrum convolved with the dust extinction curve, is found to reproduce the empirical relation of nearby starburst galaxies. As a guide to the reader's eye, two different models are also plotted in Figure 17; one has the same age as the template model (70 Myr) but a higher metallicity of 1 $Z_\odot$, and the other has the same metallicity as the template model (0.2 $Z_\odot$) but a younger age of 90 Myr.

Then, we calculate the $E(B-V)$-β_{iz} relation using the template model. The solid line of Figure 18 shows the relation for LBGs at $z = 4$, which is expressed by a linear function:

$$E(B-V) = a + b\beta_{iz}, \tag{11}$$

where $a = 0.0162$ and $b = 0.218$. Here i'- and z'-band magnitudes correspond to the average fluxes in the rest frame of 1500 ± 150 and 1800 ± 130 Å, respectively, for LBGs at $z = 4$. Note that i'- and z'-band magnitudes measure the rest-frame

[15] Note that Calzetti's attenuation curve provides the relations of $A(1600) = k_{1600}E(B-V)$ and $A(1700) = k_{1700}E(B-V)$, where $k_{1600} = 10$ and $k_{1700} = 9.6$.

fluxes of 1700 ± 170 and 2000 ± 140 Å for LBGs at $z = 3.5$, and 1400 ± 140 and 1600 ± 110 Å for LBGs at $z = 4.5$. Since β_{iz} is defined in the observed frame, this relation depends on the redshift of the galaxies. We calculate β_{iz} for the template model at $z = 3.5$, 4.5, 4.7, and 5.2, where we apply the absorption of the Lyα forest (Madau 1995) for the continuum flux at less than 1216 Å. Figure 18 displays the redshift dependence, showing that the dependence is only ±0.05 in $E(B-V)$ for galaxies with $E(B-V) \lesssim 0.5$ at $z = 3.5$–4.5, but that it exceeds $\Delta E(B-V) \simeq 0.1$ for galaxies at $z \gtrsim 4.7$. This large dependence for high-z galaxies is caused by Lyα absorption in the IGM; the Lyα forest starts entering the blue wavelength of the i'-band response function for objects at $z \gtrsim 4.7$, resulting in a systematic reddening in $i'-z'$ color (and hence a systematic increase in β_{iz}). At $z = 3.5$–4.5 the β_{iz} estimation is not affected by either the Lyα emission line at 1216 Å or the continuum emission from an older stellar population (e.g., F stars) at $\gtrsim$2700 Å. Therefore, equation (11) holds for LBGs at $z = 3.5$–4.5 with an accuracy of 0.05 mag in $E(B-V)$, but the equation does not work for LBGs at $z \gtrsim 4.7$. This is why we estimate $E(B-V)$ for *BRi*-LBGs at $z = 3.5$–4.5 alone.

5.2. *Dust Extinction of LBGs at z = 4*

We calculate the extinction of our LBGs with equations (10) and (11).[16] We show the histogram of estimated $E(B-V)$ in Figure 19. Because our Lyman break selections identify galaxies with $E(B-V) \lesssim 0.5$, as shown in Figure 15, we think that the estimated $E(B-V)$ values larger than 0.5 are spurious. In Figure 19 we limit our sample to 651 LBGs brighter than $i' = 25.5$ for the SDF and $i' = 25.0$ for the SXDF. This is because we need to measure colors up to $i'-z' \simeq 0.5$, which corresponds to $E(B-V) \simeq 0.5$, and the sample galaxies should have i' magnitudes brighter by 0.5 mag than the limiting magnitude of the z'-band image ($z'_{\rm lim} = 26.0$ for the SDF and $z'_{\rm lim} = 25.5$ for the SXDF). However, there are still systematic biases in $i'-z'$ in our LBG sample. One is that the LBG criteria preferably select bluer galaxies at fainter magnitudes, since the LBG selection needs a red $B-R$ color for the identification. This effect is also seen in the results of simulations as the difference in the red and yellow contours of the top panels in Figure 8. The other effect is that the edge of the *BRi*-LBG criteria at $1.2 < B-R < 3.0$ tends to reject red LBGs at redshifts lower than $z \simeq 4$. To correct these biases, we carry out Monte Carlo simulations similar to those described in § 3.2. We use the template model of LBGs at $z = 4$ to calculate $B-R$ and $R-i'$ colors by varying extinction over $0.0 < E(B-V) < 1.0$. We then make artificial galaxies that mimic the colors of the templates and distribute them in the original images. We detect the artificial galaxies, select them with the *BRi*-LBG criteria, and derive completeness as a function of $E(B-V)$ for four i' magnitude bins. The results are plotted in Figure 19 (*top*). Using these completeness functions, we derive completeness-corrected distributions of $E(B-V)$, which are shown by shaded histograms in Figure 19.

The mean values of $E(B-V)$ calculated from the completeness-corrected histograms are 0.18, 0.13, 0.15, and 0.14 for magnitude bins of $i' = 23.5$–24.0, 24.0–24.5, 24.5–25.0, and 25.0–25.5, respectively (Fig. 19). The mean extinction of all the *BRi*-LBGs with $i' < 25.5$ is $E(B-V) = 0.15 \pm 0.03$. Thus, the average extinction of LBGs at $z \simeq 4$ is estimated with Calzetti's law to be about a factor of 4 in luminosity at 1700 Å. Since $i' = 25.5$ corresponds to $M_{1700} = -20.8$, comparable to $M^*_{1700} = -21.0$ to -20.6 (Table 4), the mean extinction of $E(B-V) = 0.15 \pm 0.03$ is for LBGs with $M \lesssim M^*$. No significant dependence of $E(B-V)$ on the magnitude is found over $23.5 < i' < 25.5$ (corresponding to $-23 < M_{1700} < -21$). Note that these magnitudes are apparent (i.e., before extinction correction) magnitudes, and this result indicates that LBGs at $z = 4$ have no significant correlation between $E(B-V)$ and the apparent magnitude.

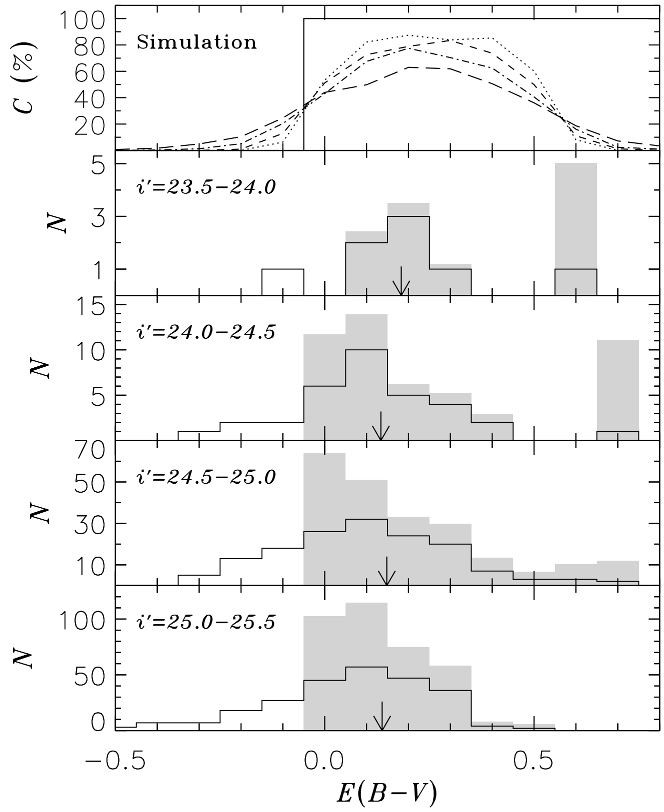

Fig. 19.—Histograms of $E(B-V)$ for four different magnitude bins for *BRi*-LBGs in the SDF and SXDF. The top panel shows the completeness of our LBG detection obtained by simulations. In the top panel, the solid line is the histogram of input objects for the simulation. The dotted, short-dashed, dot-dashed, and long-dashed lines show the completeness of LBGs with $i' = 23.75$, 24.25, 24.75, and 25.25, respectively. The other panels show the number of objects in each magnitude bin as a function of extinction. In these panels, shaded histograms correspond to measurements corrected for the completeness shown in the top panel, while open histograms show raw numbers. Arrows denote the mean value of extinction calculated from the shaded histogram for each bin. Since the completeness for objects with large extinction values, $E(B-V) > 0.55$, is less than 20%, we do not include those objects in the calculation of the mean value.

Adelberger & Steidel (2000) have obtained a similar result for LBGs at $z = 3$. It is, however, found that there is a correlation between dust extinction and (extinction-corrected) intrinsic luminosity for our LBGs. Figure 19 shows that for each magnitude bin, $E(B-V)$ spans the range of $0 \lesssim E(B-V) \lesssim 0.5$, which is larger than the statistical errors. This means that intrinsically brighter LBGs are generally more heavily attenuated by dust. The same tendency is found in LBGs at $z = 3$ by Meurer et al. (1999) and Shapley et al. (2001).

[16] The combination of eqs. (10) and (11) gives a relation between $E(B-V)$ and $i'-z'$ of $E(B-V) \simeq 0.0162 + 1.18(i'-z')$.

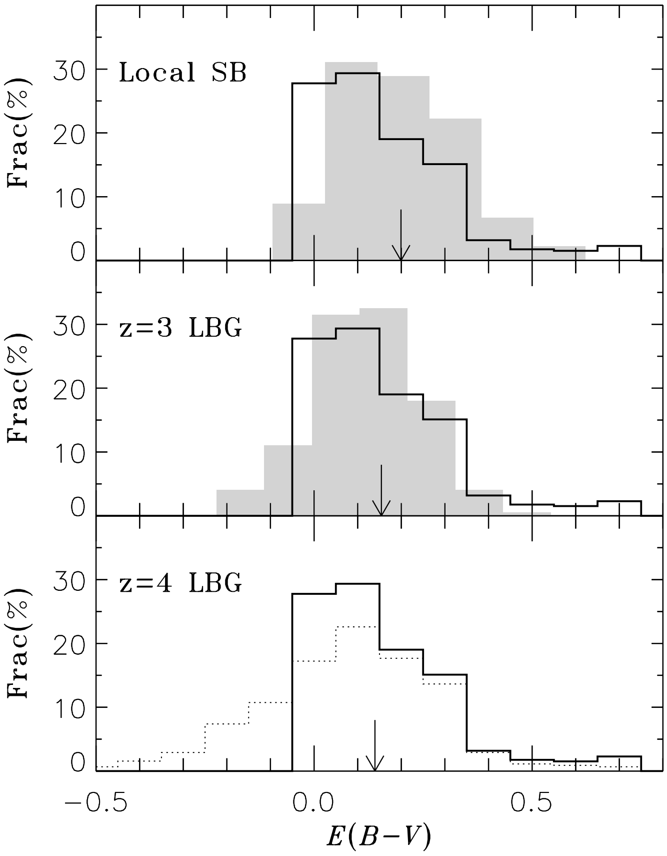

FIG. 20.—Histograms of $E(B-V)$ for galaxies at $z=0$, 3, and 4. The shaded histogram in the top panel shows the distribution of local starburst galaxies derived from *IUE* data (Meurer et al. 1999), while the shaded histogram in the middle panel is for LBGs at $z=3$ (Adelberger & Steidel 2000). The dotted histogram in the bottom panel presents our *BRi*-LBGs ($z=4$ LBGs) without correction for completeness. The open histogram in each panel shows the distribution of completeness-corrected *BRi*-LBGs down to $i'=25$ (or $M \simeq M^*$). Arrows indicate the mean values of extinction for galaxies at each redshift, which are calculated from the data over $0.0 \le E(B-V) \le 0.5$ for a fair comparison. Contamination-corrected data are used for the calculation for our *BRi*-LBGs and LBGs at $z=3$.

5.3. *Evolution of Dust Extinction at* $0 \lesssim z \lesssim 4$

We investigate the evolution of dust extinction. Figure 20 shows the histogram of $E(B-V)$ for all LBGs at $z=4$ ($i'<25.5$, i.e., $M \lesssim M^*$), together with those for local starburst galaxies (Meurer et al. 1999) and LBGs at $z=3$ (Adelberger & Steidel 2000; $R \le 25.5$, i.e., $M \lesssim M^*+1$). The $E(B-V)$ values for local galaxies and $z=3$ LBGs have also been derived from UV slopes using the extinction-β relation of Meurer et al. (1999) and the dust extinction curve of Calzetti et al. (2000). The extinction-β relation used in these papers is similar to ours, which is shown in Figure 17, with only a small difference of $\Delta A_{1600} \lesssim 0.3$, corresponding to $\Delta E(B-V) \lesssim 0.03$.

The mean dust extinctions are 0.20, 0.15, and 0.15 for local starburst galaxies, $z=3$ LBGs, and $z=4$ LBGs, respectively. If taken at face value, the mean dust extinction of LBGs at $z=3$–4 is lower than that of local starburst galaxies. However, this trend may be superficial. The sample of local starbursts is based on a combination of galaxy catalogs that are constructed by observations at various wavelengths, while the LBG samples are UV continuum–limited samples (§ 3.3). One cannot rule out the possibility that the observed trend of $E(B-V)$ is due to the selection effect that UV continuum–limited samples are likely to be biased toward dust-poor objects.

On the other hand, the sample selections of LBGs at $z=3$ and 4 are quite similar. The very small difference in the mean extinction between $z=3$ and 4 LBGs, at most $\Delta E(B-V) < 0.03$, indicates that there is no evolution in dust extinction between $z=3$ and 4.

6. EVOLUTION OF UV-LUMINOSITY DENSITY

We calculate UV-luminosity densities of our LBGs from the LFs derived in § 4. First, we integrate the LFs (Fig. 16) down to the magnitudes of the faintest LBGs in our samples (i.e., down to $M_{1700} = -19.8$, -20.5, -20.5 for *BRi*-LBGs, *Viz*-LBGs, and *Riz*-LBGs, respectively) to obtain the observed UV-luminosity densities, $\rho_{\rm UV}^{\rm obs}$, the lower limits of the UV-luminosity density. The total UV-luminosity density has to be larger than $\rho_{\rm UV}^{\rm obs}$ because of the contribution from galaxies fainter than the limiting magnitudes. In order to estimate the total UV-luminosity density, $\rho_{\rm UV}^{\rm total}$, we extrapolate the LFs down to $L=0.1L^*$. We also calculate the total UV-luminosity density by extrapolating the LFs down to $L=0$ assuming $\alpha=-1.6$, giving the upper limit of the UV-luminosity density. To derive $\rho_{\rm UV}^{\rm total}$ down to $L=0$, we use the analytic formula $\rho_{\rm UV}^{\rm total} = L^*\phi^*\Gamma(\alpha+2)$. Both $\rho_{\rm UV}^{\rm obs}$ and $\rho_{\rm UV}^{\rm total}$ for *BRi*-LBGs, *Viz*-LBGs, and *Riz*-LBGs are summarized in Table 4. The upper limits of the UV-luminosity densities are shown in parentheses in Table 4. In Table 4 we also show the results of LAEs at $z=4.86 \pm 0.03$, which are similarly calculated from the best-fit UV LF obtained in Paper II.

We discuss the evolution of the SFR (§ 6.1) and the reionization of the universe (§ 6.2) using the $\rho_{\rm UV}^{\rm total}$ estimates. We do not use $\rho_{\rm UV}^{\rm obs}$ for our discussion, since our data are still considerably shallow, and thus objects fainter than the limiting magnitudes will certainly dominate the total luminosity density. The $\rho_{\rm UV}^{\rm total}$-values for $\alpha=-2.2$ and -1.6 give an estimate of how much the $\rho_{\rm UV}^{\rm total}$-values depend on the choice of the faint-end slope. We find in Table 4 that for each sample, the $\rho_{\rm UV}^{\rm total}$-values down to $L=0.1L^*$ for the two α-values agree with each other within the errors. Furthermore, the trend that $\rho_{\rm UV}^{\rm total}$ decreases slightly from $z=4$ to 5 is consistently seen for both α-values. Thus, the error in $\rho_{\rm UV}^{\rm total}$ due to the change in α seems to be modest over a reasonable range of α. Although the choice of the faint-end slope does not much affect the results, the estimated total luminosity density is based on the large extrapolation to the observed luminosity density. We show how much this extrapolation affects the results of § 6.1.1. Since we obtain the upper limits of luminosity densities for the case of $\alpha=-1.6$, we adopt the luminosity densities from the Schechter parameters with $\alpha=-1.6$ (fixed) for the following sections.

6.1. *SFR Density*

6.1.1. *Evolution of SFR Density Based on* L_{2000}

We calculate the cosmic SFR from the UV-luminosity density, $\rho_{\rm UV}^{\rm total}$. We use the relation between the UV luminosity and the SFR given by Madau et al. (1998):

$$\mathrm{SFR}\left(M_\odot\ \mathrm{yr}^{-1}\right) = L_{\rm UV}\left(\mathrm{ergs\ s^{-1}\ Hz^{-1}}\right)/\left(8\times10^{27}\right), \qquad (12)$$

where $L_{\rm UV}$ is the UV luminosity measured at 1500–2800 Å.[17] This relation assumes that galaxies have the Salpeter IMF with

[17] The conversion factor in eq. (12) is 8.0×10^{27} for the luminosity at 1500 Å and 7.9×10^{27} for the luminosity at 2800 Å (Madau et al. 1998).

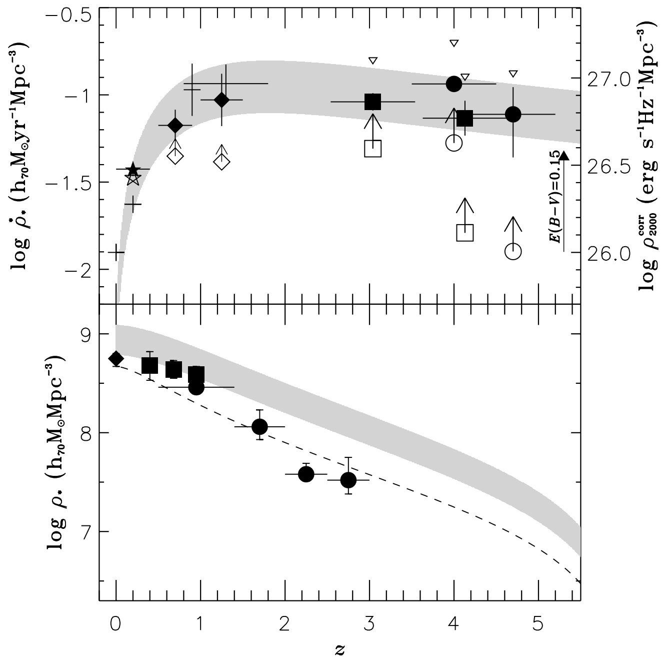

FIG. 21.—*Top*: Cosmic SFR as a function of redshift. The cosmic SFR is calculated from the luminosity density at $\simeq$2000 Å, $\rho_{2000}^{\rm corr}$, estimated from $\rho_{\rm UV}^{\rm tot}$ and $\rho_{\rm UV}^{\rm obs}$, which are corrected for a dust extinction of $E(B-V)=0.15$, whose value is indicated by a long arrow (see § 5). Circles, squares, diamonds, and stars show values for LBGs at $z=4-5$ (present study), LBGs at $z=3-4$ (Steidel et al. 1999), galaxies at $z\sim 1$ (Cowie et al. 1996), and galaxies at $z\simeq 0$ (Sullivan et al. 2000), respectively. Filled symbols indicate the total cosmic SFRs calculated by integrating the LFs down to $L=0.1L^*$, and open symbols with arrows show lower limits, i.e., contributions by only actually detected galaxies. The differences between filled symbols and open symbols are due to the contributions from faint galaxies below the detection limits. Open triangles plotted at $z>3$ indicate the upper limits that are calculated by integrating the LFs down to $L=0$. The plus signs at $z=0$, 0.2, 0.9, and 1.3 are cosmic SFRs derived from the Hα-luminosity density by Gallego et al. 1995, Tresse & Maddox 1998, Glazebrook et al. 1999, and Yan et al. 1999, respectively. Note that the cosmic SFRs estimated from $\rho_{2000}^{\rm corr}$ (*filled symbols*) are comparable to those calculated from the Hα-luminosity density (*plus signs*) at $z=0-1$. The shaded region shows the approximate evolution of the cosmic SFR obtained from a fit of an analytic function (see text for details) to the data points. *Bottom*: Stellar mass density as a function of redshift. The shaded region indicates the stellar mass density accumulated from $z=6$, which is calculated from the cosmic SFR shown as the shaded region in the top panel. The dashed line shows the stellar mass density calculated from the cosmic SFR of observed galaxies alone (i.e., the open symbols in the top panel). The circles, squares, and diamonds denote the stellar mass density derived from the stellar mass function by Cole et al. (2001), Cohen (2002), and Dickinson et al. (2003), respectively.

solar metallicity. This conversion is insensitive to the difference in the star formation history, especially for the far-UV luminosity at $\lesssim$2000 Å, since UV fluxes are produced by massive OB stars whose lifetimes are $\lesssim 2\times 10^7$ yr (Madau et al. 1998). Figure 21 shows the cosmic SFRs of $z=4$–5 LBGs in our sample, together with those of galaxies at $z=0$ (Sullivan et al. 2000), $z=0$–1 (Cowie et al. 1996), and $z=3$–4 (Steidel et al. 1999). These cosmic SFRs (and UV-luminosity densities) have been corrected for the same amount of dust correction, $E(B-V)=0.15$, since there is no significant change in the observed $E(B-V)$ value over $z=0-4.5$ (§ 5.3). We also show the cosmic SFRs at $z=0$, 0.2, 0.9, and 1.3 estimated from the Hα-luminosity density given by Gallego et al. (1995), Tresse & Maddox (1998), Glazebrook et al. (1999), and Yan et al. (1999), respectively. Note that the cosmic SFRs estimated from the UV-luminosity density with dust correction are comparable to those calculated from the Hα-luminosity density. Figure 21 indicates that there is no significant change, or is possibly a slight decline, in the cosmic SFR from $z\simeq 1$ up to $\simeq$5. The possible decline from $z=4$ to 5 is due to the decrease in luminosity density found in § 7.2.

In Figure 21 we also plot the SFR calculated from $\rho_{\rm UV}^{\rm obs}$ (*open circles*). Since $\rho_{\rm UV}^{\rm obs}$ is the UV-luminosity density contributed by the bright portion of LFs for which data exist, these are robust lower limits of the SFR. We find from our data at $z=4$ that the cosmic SFR is almost constant from $z\simeq 1$ to 4.5, even when we use $\rho_{\rm UV}^{\rm obs}$ instead of $\rho_{\rm UV}^{\rm tot}$. It should be noted that the lower limit at $z=4$ obtained by Steidel et al. (1999) is much lower than ours, based on $\rho_{\rm UV}^{\rm obs}$, because of their shallow data. Our data have largely improved the robust lower limit of the cosmic SFR at $z=4$. On the other hand, the lower limit derived for our $z=5$ LBGs is not high enough to reject a large decline of the cosmic SFR at $z=5$. However, the true cosmic SFR at $z=5$ is presumably high, as the estimate from $\rho_{\rm UV}^{\rm tot}$ indicates, since we find at $z\lesssim 1$ a good agreement between the cosmic SFRs derived from total Hα-luminosity densities and those based on UV-luminosity densities that are estimated from extrapolated LFs with dust-extinction correction. We fit the cosmic SFR data, including those based on Hα-luminosity density, with the analytic function of redshift given in Cole et al. (2001), cosmic SFR $=(a+bz)/[1+(z/c)^d]\ h_{70}^{-2}\ M_\odot\ {\rm yr}^{-1}$ Mpc^{-3}, and obtain $a=0.0039$, $b=0.13$, $c=1.6$, and $d=1.8$. We show the best-fit function with errors by the shaded region in Figure 21.

6.1.2. *Stellar Mass Assembly History*

We estimate the stellar mass density accumulated from $z=6$, using the best-fit function of the cosmic SFR obtained in § 6.1.1. We show the stellar mass density calculated by integrating the cosmic SFR over cosmic time as a function of redshift by the shaded region in Figure 21 (*bottom*), together with those measured directly from the stellar mass function of galaxies at $z=0$–3 (Cole et al. 2001; Cohen 2002; Dickinson et al. 2003). Since the cosmic SFRs at high-z are calculated from an extrapolation of the LF, they may overestimate the real cosmic SFRs if the true LFs have flatter slopes. Thus, we also estimate the lower limits of the stellar mass density from the observed luminosity densities (Fig. 21, *top*, *open symbols*). The lower limit values are connected by the dashed line in Figure 21.

At $z=0$–1, the stellar mass densities derived directly from the stellar mass functions are consistent with those calculated from the cosmic SFRs (both the total densities $\rho_{\rm UV}^{\rm total}$ and the lower limits $\rho_{\rm UV}^{\rm obs}$) within the uncertainties. At $z=1$–3, however, the stellar mass densities based on the stellar mass functions are as low as the lower limits calculated from $\rho_{\rm UV}^{\rm obs}$ and about a factor of 3 lower than the total densities calculated from $\rho_{\rm UV}^{\rm total}$. There are at least four possible reasons for this discrepancy. First, the stellar mass densities obtained by Dickinson et al. (2003) may suffer from a large cosmic variance because they are based on data of the HDF-N, a very small patch of the sky. Second, the stellar population synthesis models used to derive the cosmic SFRs and the stellar mass functions may not be appropriate for high-z galaxies. For example, both our analysis and that of Dickinson et al. (2003) adopt the Salpeter IMF. However, it is possible that high-z galaxies have a different IMF (e.g., a top-heavy IMF). Third, Dickinson et al. (2003) assume a constant mass-to-luminosity ratio for faint galaxies whose stellar masses are not measured by fitting their stellar synthesis models. If, however, the actual mass-to-luminosity ratio increases with decreasing luminosity, the stellar mass densities obtained by Dickinson et al. (2003) are underestimates of the true values. Fourth, while we assume that the dust extinction of LBGs is constant with luminosity, LBGs fainter than the detection limits may have smaller extinction. Such a decrease in $E(B-V)$ could largely change the total cosmic SFR, since the contribution to the cosmic SFR from LBGs fainter than the detection limits is significant.

6.2. *Contribution to the Reionization of the Universe*

The IGM has been ionized since at least $z = 6$ (Becker et al. 2001; Fan et al. 2002). Since a large number of ionized hydrogen recombines in a relatively short timescale,[18] ionizing photons have to be supplied by objects at each epoch to keep the IGM ionized. Madau et al. (1999) give a formula to calculate the critical rate of ionizing photons, $\dot{N}_{\rm ion}^{\rm cr}$, required to maintain the ionization of the IGM. The original formula is given in the Einstein–de Sitter cosmology, and we rewrite their formula, which can be applied to our Λ-cosmology ($h = 0.7$, $\Omega_m = 0.3$, $\Omega_\Lambda = 0.7$) with an acceptable accuracy at $3 \lesssim z \lesssim 6$, as

$$\dot{N}_{\rm ion}^{\rm cr} = \left(10^{51.0}\ {\rm s^{-1}\ Mpc^{-3}}\right) C_{30} \left(\frac{1+z}{6}\right)^3 \left(\frac{\Omega_m h^2}{0.02}\right)^2, \quad (13)$$

where C_{30} is the ionized hydrogen clumping factor normalized by 30. The fiducial value for this clumping factor is $C_{30} = 1$. The main uncertainty in this critical rate originates from this clumping factor, which is estimated to be of order ± 0.2 dex (Madau et al. 1999). We plot the critical rate as a function of redshift in Figure 22, together with the emission rate of ionizing photons from QSOs shown in Madau et al. (1999). Figure 22 indicates that the QSOs' production rate of ionizing photons, $\dot{N}_{\rm ion}({\rm QSO})$, is less than the critical rate at $z \gtrsim 3.6$.

Since the number density of low-luminosity active galactic nuclei at high-z ($z \sim 3$) is much lower than that of LBGs at similar redshifts (3%; Steidel et al. 2002), the deficit of ionizing photons should be supplied from massive stars in galaxies. We estimate the emission rate of ionizing photons per unit volume from galaxies, $\dot{N}_{\rm ion}({\rm gal})$, at $z = 4$ and 5. The emission rate is related to the cosmic SFR, i.e., the SFR density (SFRD) by

$$\dot{N}_{\rm ion}({\rm gal}) = C f_{\rm esc} {\rm SFRD}\left(M_\odot\ {\rm yr^{-1}\ Mpc^{-3}}\right)\ {\rm numbers^{-1}\ Mpc^{-3}}, \quad (14)$$

where C is a conversion factor, $f_{\rm esc}$ is the escape fraction of ionizing photons, and SFRD is the SFR of galaxies per unit volume (Madau et al. 1999). Madau et al. (1999) estimate $C = 10^{53.1}$. We use equation (12) to calculate the SFR.

Among the above parameters, the escape fraction of ionizing photons is unknown. Here we give a constraint on the escape fraction for LBGs at $z = 4$ and 5 using our data as follows: Since the IGM at $z \lesssim 6$ is ionized (Becker et al. 2001), the sum of ionizing photons from QSOs and galaxies should at least exceed the critical rate at $z \lesssim 6$:

$$\dot{N}_{\rm ion}^{\rm cr} < \dot{N}_{\rm ion}({\rm gal}) + \dot{N}_{\rm ion}({\rm QSO}). \quad (15)$$

[18] The recombination timescale depends on the density of the IGM and thus on redshift. The recombination timescale at $z = 3$ is estimated to be $\approx$300 Myr (Madau et al. 1999).

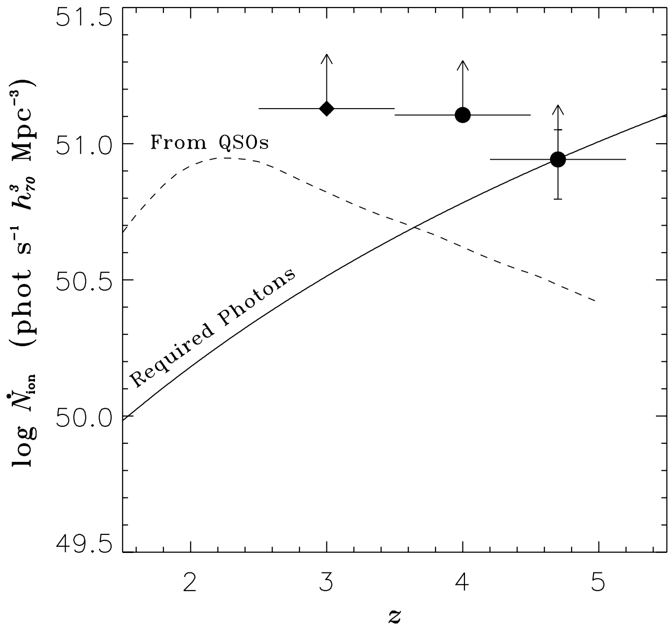

FIG. 22.—UV ionizing photon density ($\dot{N}_{\rm ion}$) of the universe at $z = 2-5$. The solid line indicates the $\dot{N}_{\rm ion}$ required to maintain the ionization of the IGM predicted by Madau et al. (1999). The dashed line shows the $\dot{N}_{\rm ion}$ contributed from QSOs. The diamond and circles denote the sum of the ionizing photons from QSOs and galaxies, where the ionizing photons from galaxies are estimated from LBGs at $z = 3$ (Steidel et al. 1999) and at $z = 4$ and 5 (present data) assuming $f_{\rm esc} = 0.13$. This figure visualizes the fact that an average $f_{\rm esc} \gtrsim 0.13$ is required for galaxies at $z = 4.7$ in order to maintain ionization.

First, we consider the escape fraction of our LBGs at $z = 5$. We estimate the critical rate using equation (13) to be $\dot{N}_{\rm ion}^{\rm cr} = 8.8^{+5.1}_{-3.2} \times 10^{50}$, and we find $\dot{N}_{\rm ion}({\rm QSO}) = 3.0 \times 10^{50}$ (Madau et al. 1999). On the other hand, the number density of ionizing photons from galaxies is calculated to be $\dot{N}_{\rm ion}({\rm gal}) = 4.4 \pm 1.9 \times 10^{51} f_{\rm esc}$. Substituting these values for equation (15), we find $f_{\rm esc} > 0.13^{+0.13}_{-0.09}$ for LBGs at $z = 5$. Similarly we obtain $f_{\rm esc} > 0.02^{+0.05}_{-0.02}$ for LBGs at $z = 4$. Note that the errors in $f_{\rm esc}$ include the uncertainty in C_{30}, ± 0.2 dex. Thus, we place a moderately significant constraint on the escape fraction for LBGs at $z = 5$ but not for LBGs at $z = 4$. Throughout the above discussion, we use the upper limits of the luminosity density (values in parentheses in Table 4) for LBGs at $z = 4$ and 5, which are obtained by integrating the LFs down to $L = 0$. Since $f_{\rm esc}$ decreases with the luminosity density, the $f_{\rm esc}$ values calculated from these luminosity densities are regarded as conservative lower limits. We conclude that the escape fraction should be $f_{\rm esc} \gtrsim 0.13$ for LBGs at $z = 5$. We plot in Figure 22 the sum of the number densities of ionizing photons from QSOs and galaxies at $z = 3-5$, assuming the lower limit of the escape fraction to be $f_{\rm esc} = 0.13$.

7. DISCUSSION

7.1. *LFs and Dust Extinction of LBGs at* $z = 4-5$

LFs of LBGs show that the number of bright galaxies decreases significantly from $z = 4$ to 5 but little from $z = 3$ to 4. We find that the slope of the LF may steepen from $z = 3$ to 4. Our findings indicate that most of the bright ($M_{1700} \lesssim -22$) galaxies appear between $z = 4$ and 5, while faint ($M_{1700} \gtrsim -22$) galaxies dominate in number density at $z \gtrsim 4$. We find in Figure 16 that while our LF at $z = 4$ agrees well with that derived by Steidel et al. (1999), our LF at $z = 5$ is different from that obtained by Iwata et al. (2003), who claim that the

LF at $z = 5$ is similar to that at $z = 3$. Thus, there is a discrepancy between our findings and theirs. We examine the cause of this discrepancy. First of all, the field variance may be large for such bright LBGs, since the number of detected bright LBGs is as small as $\sim$20. However, we find an excellent consistency between the LFs derived from the SDF and the SXDF. Thus, the field variance is probably not the main reason for this discrepancy. Second, it is possible that the selection criteria of Iwata et al. (2003) would take a large number of contaminants in their LBG sample, as discussed in § 3.1, resulting in a number density of bright LBGs larger than ours.

We estimate the SFR of bright LBGs with $M_{1700} \lesssim -22$ with equation (12) to be $\mathrm{SFR_{raw}} \gtrsim 30\ h_{70}^{-2}\ M_\odot\ \mathrm{yr}^{-1}$ (see the upper abscissa axis of Fig. 16 for the correspondence between M_{1700} and $\mathrm{SFR_{raw}}$). Since the UV luminosity of these LBGs has a dust extinction of $E(B-V) \simeq 0.15$, the extinction-corrected SFR is about a factor of 4 larger than $\mathrm{SFR_{raw}}$ (§ 5.2). Thus, LBGs with $M_{1700} \lesssim -22$ have an intrinsic SFR of $\gtrsim 100\ h_{70}^{-2}\ M_\odot\ \mathrm{yr}^{-1}$. The deficit of $M_{1700} \lesssim -22$ LBGs at $z = 5$ indicates that the number density of galaxies with high SFR of $\gtrsim 100\ h_{70}^{-2}\ M_\odot\ \mathrm{yr}^{-1}$ drops from $z = 4$ to 5.

Our LFs are derived for UV luminosity or, equivalently, SFR. In general, galaxies with larger sizes and higher star formation efficiencies have higher SFRs. Thus, our findings imply that large galaxies are formed by subsequent mergers of small galaxies and/or that star formation efficiency increases from $z = 5$ to 3. The former interpretation supports the picture of hierarchical clustering (e.g., Baugh et al. 1998; Kauffmann et al. 1999; Weinberg et al. 2002), in which galaxies experience a number of mergers. On the other hand, the latter interpretation is not consistent with predictions from numerical simulations of hierarchical clustering. Since the cooling efficiency increases with the density of gas in dark halos, hot gas cools more efficiently at higher redshifts, resulting in a higher star formation efficiency at a higher redshift (Hernquist & Springel 2003), which is opposite to the observed evolution. Thus, a decrease in the number density of dark halos predicted by the former scenario should explain the observed evolution of the LF at bright magnitudes. We calculate the cumulative number density of massive dark halos down to $10^{12}\ M_\odot$, at which LBGs with $M_{1700} \lesssim -20.5$ are expected to reside (see the companion paper, Paper VI), and find that the number density of these massive halos is 44% (at $z = 4$) and 16% (at $z = 5$) of that at $z = 3$. This decrease is roughly consistent with the observed decrease of bright LBGs in the number density from $z = 3$ to 5.

The slope of the LF at $z = 4$ is estimated to be $\alpha = -2.2 \pm 0.2$. Since the faintest LBGs in our sample are as bright as $M^* + 1$, the estimated slope should have large systematic errors. If taken at face value, the faint-end slope of the LF at $z = 4$ is steeper than that at $z = 3$ ($\alpha = -1.6$; Steidel et al. 1999). Yan et al. (2003) report that the faint-end slope of the LF for LBGs at $z \simeq 6$ may be as steep as $\alpha \sim -2$ from their deep *Hubble Space Telescope* ACS data. Thus, the slope of the LF for LBGs may steepen at $z \gtrsim 4$. However, these results might conflict with model predictions. The number density of faint galaxies is predicted to decrease right after the reionization ($z \simeq 6$; Becker et al. 2001), since the reionization increases the Jeans mass of the IGM and thus the minimum mass of forming galaxies (Gnedin & Ostriker 1997; Miralda-Escudé & Rees 1998).

The average extinction of LBGs at $z = 4$, $E(B-V) = 0.15 \pm 0.03$, is the same as that of LBGs at $z = 3$ derived by Adelberger & Steidel (2000) from their large sample. Furthermore, the dependence of extinction on intrinsic luminosity for $z = 4$ LBGs is similar to that for $z = 3$ LBGs. This means that the average dust properties are the same between $z = 3$ and $z = 4$ LBGs. Interestingly, Ferguson et al. (2002) find that most of the LBGs seen at $z = 3$ started star formation after $z = 4$, i.e., LBGs at $z = 3$ are not descendants of LBGs at $z = 4$. Thus, LBGs at $z = 3$ and 4 may be similarly young, and so have a similar amount of dust.

7.2. *UV-Luminosity Density and Escape Fraction*

We compare in Figure 21 the luminosity densities of LBGs at $z = 4-5$ in our samples with those at $z = 3$ and 4, which are calculated from the LFs given in Steidel et al. (1999). Figure 21 shows that the UV-luminosity density of LBGs does not change significantly from $z = 3$ to 5. The luminosity density of LBGs is $\rho_{\mathrm{UV}}^{\mathrm{total}} = 1.9 \pm 0.2 \times 10^{26}$, $2.0 \pm 0.2 \times 10^{26}$, and $1.6 \pm 0.7 \times 10^{26}$ ergs s^{-1} Hz^{-1} Mpc^{-3} (see Table 4) for $z = 3$, 4, and 5, respectively, where the value at $z = 4$ is the mean of our measurement and that of Steidel et al. Thus, the ratios of the UV-luminosity density at $z = 4$ and 5 to that at $z = 3$ are $\rho_{\mathrm{UV}}(z=4)/\rho_{\mathrm{UV}}(z=3) = 1.0 \pm 0.2$ and $\rho_{\mathrm{UV}}(z=5)/\rho_{\mathrm{UV}}(z=3) = 0.8 \pm 0.4$. The total UV-luminosity density may slightly decrease toward $z = 5$, but the amount of the decrease is 20% at most. Although the number density of bright LBGs ($M_{1700} \lesssim -22$) significantly decreases toward $z = 5$ (Fig. 16), the total UV-luminosity density does not largely change. This is because the total UV-luminosity density is mainly contributed by LBGs fainter than $M_{1700} \sim -22$.

The luminosity density of LAEs at $z = 4.86$ is calculated to be 9.6×10^{25} ergs s^{-1} Hz^{-1} Mpc^{-3} with the UV LF obtained by Paper II in the same manner as for LBGs (Table 4). The ratio of the UV-luminosity density of LAEs to that of LBGs is $\rho_{\mathrm{UV}}(\mathrm{LAE})/\rho_{\mathrm{UV}}(\mathrm{LBG}) \simeq 0.6$ at $z \simeq 5$. Since LBG samples are UV-luminosity–limited samples (§ 3.3), the UV-luminosity density derived from the LBG LF represents the UV-luminosity density of the whole galaxy population (if an appropriate extrapolation of the LF down to a very faint luminosity is made). Thus, about 60% of the cosmic UV-luminosity density (or cosmic SFR) at $z \sim 5$ is contributed by galaxies identified as LAEs.

Figure 21 shows that the cosmic SFR is constant from $z \sim 1$ to 5. This result agrees with that obtained by Iwata et al. (2003), although the bright end of the LF is significantly different between ours and that of Iwata et al. (2003). This coincidence indicates that faint LBGs ($\mathrm{SFR} \sim 1\ h_{70}^{-2}\ M_\odot\ \mathrm{yr}^{-1}$) contribute much more to the cosmic SFR than bright LBGs ($\mathrm{SFR} \gtrsim 100\ h_{70}^{-2}\ M_\odot\ \mathrm{yr}^{-1}$). The constant cosmic SFR from $z =$ 1–5 is consistent with predictions of numerical simulations. Ascasibar et al. (2002) have found from numerical simulations that the cosmic SFR shows almost no drop over $2 < z < 5$ and that star formation is a gradual process with no characteristic epoch. Nagamine et al. (2000) have predicted from hydrodynamic simulations that the cosmic SFR shows a moderate plateau between $z = 1$ and 3 and a gradual decrease beyond $z = 3$ up to $z = 5$ by $\sim$0.4 dex. The cosmic SFR at $z = 3-5$ is about 5 times larger than that at $z = 0$ (Fig. 21, *top*). The star formation is very active at these high redshifts, but the accumulated stellar mass density (Fig. 21, *bottom*) at $z = 3$ is just 1/10 of the present-day stellar mass density. Since the cosmic time between $z = 5$ and 3 is much shorter than that between $z = 3$ and 0 (1 vs. 10 Gyr), the majority of stars are produced not at these high redshifts ($z = 3-5$) but at lower redshifts ($z < 3$).

We calculate the number density of ionizing photons contributed by LBGs (§ 6.2). We give a lower limit for the escape fraction of ionizing photons for LBGs at $z = 4.7$ ($f_{\rm esc} \gtrsim 0.13$). It should be noted here that this $f_{\rm esc}$ value is inferred from a combination of the estimated UV luminosity for LBGs and a model of ionization. In this sense, our method intrinsically has a large ambiguity, since most of the $f_{\rm esc}$ values given in the literature are based on direct measurements of the Lyman continuum in spectra (see below). Nevertheless, our results are useful, giving a new, independent constraint on $f_{\rm esc}$.

Steidel et al. (2001) have found that the average spectrum of LBGs at $z \simeq 3.4$ has a Lyman continuum and that the flux ratio between the UV continuum at 1500 Å and the Lyman continuum at 900 Å is $f_{900}/f_{1500} = 1/4.6$ after correction for IGM absorption. This flux ratio corresponds to an escape fraction $f_{\rm esc} \sim 3(1/4.6) = 0.65$, where the factor of 3 comes from the assumed shape of the intrinsic spectrum (see Giallongo et al. 2002). On the other hand, Giallongo et al. (2002) have found no Lyman continuum flux in their two LBGs at $z = 3$, and they set an upper limit for the escape fraction of $f_{\rm esc} < 0.16$. The measurement of Giallongo et al. (2002) is not consistent with that of Steidel et al. (2001). Giallongo et al. (2002) discuss that this inconsistency may be due to differences in sample selection. In either case, our estimate $f_{\rm esc} \gtrsim 0.13$ does not seriously conflict with these two previous measurements, if the escape fraction does not change from $z = 5$ to 3. The escape fraction of LBGs is probably not smaller than $\sim$10%.

We compare these $f_{\rm esc}$ values with those of present-day galaxies. Leitherer et al. (1995) have given an upper limit for four nearby starbursts using far-UV spectra. The values they have obtained are $f_{\rm esc} \leq 0.0095$, 0.017, 0.048, and 0.15. Hurwitz et al. (1997) reanalyzed the data of Leitherer et al. (1995) to obtain higher values: $f_{\rm esc} \leq 0.032$, 0.052, 0.11, and 0.57. Tumlinson et al. (1999) have found $f_{\rm esc} \leq 0.02$ for NGC 3067. The escape fraction of the Milky Way has been estimated to be $f_{\rm esc} \sim 0.06$ by Bland-Hawthorn & Maloney (1999). The average $f_{\rm esc}$ seems to be $f_{\rm esc} \lesssim 0.1$ for present-day galaxies. This implies that the escape fraction of LBGs at $z = 3$–5 is larger than that of star-forming galaxies at $z = 0$.

8. CONCLUSIONS

We have made large samples of 2600 Lyman break galaxies (LBGs) at $z = 3.5$–5.2 detected in deep ($i' \simeq 27$) and wide-field (1200 arcmin^2) data of the Subaru Deep Field (SDF) and the Subaru/*XMM-Newton* Deep Field (SXDF) and have studied their photometric properties. The major findings of our study are summarized as follows:

1. We find that our selection criteria for LBGs can isolate about 90% of all galaxies in a targeted redshift range, if the galaxies have sufficiently high S/N (Fig. 14 in § 3.3). Thus, our LBG samples are regarded as nearly UV magnitude–limited samples of high-z galaxies. The missed 10% of the galaxies are galaxies attenuated heavily by dust [$E(B-V) \gtrsim 0.4$].

2. We derive LFs of LBGs at $\langle z \rangle = 4.0$, 4.7, and 4.9 in § 4. We find no cosmic variance between the SDF and the SXDF. Then, comparing them with that at $\langle z \rangle = 3$ (Steidel et al. 1999), we find that while the LF of LBGs does not show a large change over $z = 3$ and 4, as reported by Steidel et al. (1999), the number density of bright galaxies with $M_{1700} < -22$ (or galaxies with a high SFR of $\gtrsim 100\ h_{70}^{-2}\ M_{\odot}\ {\rm yr}^{-1}$ with extinction correction) decreases by an order of magnitude from $z = 4$ to 5. We also find that the faint-end slope of the LF may be steeper at $z = 4$ than at $z = 3$.

3. We estimate the dust extinction of LBGs at $z = 4 \pm 0.5$ from the UV-continuum slope measured from $i' - z'$ color (§ 5). We do not measure the dust extinction of LBGs at $z > 4.5$, because $i' - z'$ measurements are significantly affected by absorption of the IGM and by Lyα emission (Fig. 18 in § 5.1). We find that LBGs with $M < M^*$ ($\simeq -21$) have $E(B-V) = 0.15 \pm 0.03$ on average, if a completeness correction is made to the sample, and that the amount of extinction depends not on the apparent luminosity but on the intrinsic luminosity. We find no evolution in dust extinction between $z = 3$ and 4.

4. We calculate the UV-luminosity density at 1700 Å for our LBGs by integrating the LFs derived in § 4.1. Then we estimate the cosmic SFRs at $z = 4$ and 5 from the UV-luminosity density and compare them with those at $z < 4$ given by various authors. We find that the UV-luminosity density at 1700 Å, $\rho_{\rm UV}$, does not significantly change from $z = 3$ to 5, i.e., $\rho_{\rm UV}(z=4)/\rho_{\rm UV}(z=3) = 1.0 \pm 0.2$ and $\rho_{\rm UV}(z=5)/\rho_{\rm UV}(z=3) = 0.8 \pm 0.4$. Comparing the UV-luminosity density of LBGs at $z = 5$ with that of LAEs at $z = 4.9$ calculated from the data of Paper II, we obtain $\rho_{\rm UV}({\rm LAE})/\rho_{\rm UV}({\rm LBG}) \simeq 0.6$. It implies that about half ($\simeq$60%) of the star formation at $z \sim 5$ occurs in LAEs.

5. We derive the cosmic SFR at $z \sim 4$ and 5 from $\rho_{\rm UV}$ of our LBGs (§ 6.1) with the correction for dust extinction of $E(B-V) = 0.15$ obtained in § 5.2. Combining our measurements with those at $z \lesssim 3$ given in the literature, we find that the cosmic SFR is almost constant, or shows a possible decline, from $z = 3$ to 5. We then estimate the stellar mass density at $z \lesssim 5$ by integrating the cosmic SFR over time and find that at $z \sim 1$–3 the stellar mass density based on the cosmic SFR exceeds that derived directly from the stellar mass function by a factor of 3, while the two estimates agree at $z \lesssim 1$.

6. We estimate the production rate of ionizing photons for LBGs from $\rho_{\rm UV}$ using the model proposed by Madau et al. (1999) (§ 6.2). We find that more than $\simeq$13% of ionizing photons produced by massive stars should escape from LBGs at $z \simeq 5$ (i.e., $f_{\rm esc} \gtrsim 0.13$) in order to keep the IGM ionized.

We would like to thank the Subaru Telescope staff for their invaluable help in commissioning the Suprime-Cam that made these difficult observations possible. We thank the referee, Patrick McCarthy, for his constructive suggestions and comments that improved this article. M. O. acknowledges support from the Japan Society for the Promotion of Science (JSPS) through JSPS Research Fellowships for Young Scientists.

REFERENCES

Adelberger, K. L., & Steidel, C. C. 2000, ApJ, 544, 218
Ascasibar, Y., Yepes, G., Gottlöber, S., & Müller, V. 2002, A&A, 387, 396
Baugh, C. M., Cole, S., Frenk, C. S., & Lacey, C. G. 1998, ApJ, 498, 504
Becker, R. H., et al. 2001, AJ, 122, 2850
Benítez, N. 2000, ApJ, 536, 571
Bertin, E., & Arnouts, S. 1996, A&AS, 117, 393
Bland-Hawthorn, J., & Maloney, P. R. 1999, ApJ, 510, L33
Brinchmann, J., & Ellis, R. S. 2000, ApJ, 536, L77
Bruzual, G., & Charlot, S. 2003, MNRAS, 344, 1000
Bruzual A., G., & Charlot, S. 1993, ApJ, 405, 538

Calzetti, D. 2001, PASP, 113, 1449
Calzetti, D., Armus, L., Bohlin, R. C., Kinney, A. L., Koornneef, J., & Storchi-Bergmann, T. 2000, ApJ, 533, 682
Calzetti, D., Kinney, A. L., & Storchi-Bergmann, T. 1994, ApJ, 429, 582
Cohen, J. G. 2002, ApJ, 567, 672
Cole, S., et al. 2001, MNRAS, 326, 255
Coleman, G. D., Wu, C.-C., & Weedman, D. W. 1980, ApJS, 43, 393
Connolly, A. J., Csabai, I., Szalay, A. S., Koo, D. C., Kron, R. G., & Munn, J. A. 1995, AJ, 110, 2655
Cowie, L. L., Songaila, A., Hu, E. M., & Cohen, J. G. 1996, AJ, 112, 839
Dickinson, M. 2000, Royal Soc. London Philos. Trans. Ser. A, 358, 2001
Dickinson, M., Papovich, C., Ferguson, H. C., & Budavári, T. 2003, ApJ, 587, 25
Fan, X., Narayanan, V. K., Strauss, M. A., White, R. L., Becker, R. H., Pentericci, L., & Rix, H. 2002, AJ, 123, 1247
Ferguson, H. C., Dickinson, M., & Papovich, C. 2002, ApJ, 569, L65
Fernández-Soto, A., Lanzetta, K. M., & Yahil, A. 1999, ApJ, 513, 34
Fontana, A., D'Odorico, S., Poli, F., Giallongo, E., Arnouts, S., Cristiani, S., Moorwood, A., & Saracco, P. 2000, AJ, 120, 2206
Franx, M., et al. 2003, ApJ, 587, L79
Fukugita, M., Shimasaku, K., & Ichikawa, T. 1995, PASP, 107, 945
Furusawa, H. 2002, Ph.D. thesis, Univ. Tokyo
Furusawa, H., Shimasaku, K., Doi, M., & Okamura, S. 2000, ApJ, 534, 624
Gallego, J., Zamorano, J., Aragón-Salamanca, A., & Rego, M. 1995, ApJ, 455, L1
Giallongo, E., Cristiani, S., D'Odorico, S., & Fontana, A. 2002, ApJ, 568, L9
Glazebrook, K., Blake, C., Economou, F., Lilly, S., & Colless, M. 1999, MNRAS, 306, 843
Gnedin, N. Y., & Ostriker, J. P. 1997, ApJ, 486, 581
Gunn, J. E., & Stryker, L. L. 1983, ApJS, 52, 121
Gwyn, S. D. J., & Hartwick, F. D. A. 1996, ApJ, 468, L77
Hernquist, L., & Springel, V. 2003, MNRAS, 341, 1253
Hu, E. M., Cowie, L. L., McMahon, R. G., Capak, P., Iwamuro, F., Kneib, J.-P., Maihara, T., & Motohara, K. 2002, ApJ, 568, L75
Hurwitz, M., Jelinsky, P., & Dixon, W. V. D. 1997, ApJ, 481, L31
Iwata, I., Ohta, K., Tamura, N., Ando, M., Wada, S., Watanabe, C., Akiyama, M., & Aoki, K. 2003, PASJ, 55, 415
Kashikawa, N., et al. 2002, PASJ, 54, 819
———. 2003, AJ, 125, 53 (Paper III)
Kauffmann, G., Colberg, J. M., Diaferio, A., & White, S. D. M. 1999, MNRAS, 307, 529
Kodaira, K., et al. 2003, PASJ, 55, L17
Labbé, I., et al. 2003, AJ, 125, 1107
Landolt, A. U. 1992, AJ, 104, 340
Lanzetta, K. M., Yahil, A., & Fernández-Soto, A. 1996, Nature, 381, 759
Leitherer, C., Ferguson, H. C., Heckman, T. M., & Lowenthal, J. D. 1995, ApJ, 454, L19
Lowenthal, J. D., et al. 1997, ApJ, 481, 673
Madau, P. 1995, ApJ, 441, 18
Madau, P., Ferguson, H. C., Dickinson, M. E., Giavalisco, M., Steidel, C. C., & Fruchter, A. 1996, MNRAS, 283, 1388
Madau, P., Haardt, F., & Rees, M. J. 1999, ApJ, 514, 648
Madau, P., Pozzetti, L., & Dickinson, M. 1998, ApJ, 498, 106
Maihara, T., et al. 2001, PASJ, 53, 25 (Paper I)
Massarotti, M., Iovino, A., Buzzoni, A., & Valls-Gabaud, D. 2001, A&A, 380, 425
Meurer, G. R., Heckman, T. M., & Calzetti, D. 1999, ApJ, 521, 64
Miralda-Escudé, J., & Rees, M. J. 1998, ApJ, 497, 21
Miyazaki, S., et al. 2002, PASJ, 54, 833
Monet, D. E. A. 1998, The PMM USNO-A2.0 Catalog (Washington, DC: USNO)
Motohara, K., et al. 2002, PASJ, 54, 315
Nagamine, K., Cen, R., & Ostriker, J. P. 2000, ApJ, 541, 25
Oke, J. B. 1974, ApJS, 27, 21
———. 1990, AJ, 99, 1621
Ouchi, M. 2003, Ph.D. thesis, Univ. Tokyo
Ouchi, M., Yamada, T., Kawai, H., & Ohta, K. 1999, ApJ, 517, L19
Ouchi, M., et al. 2001, ApJ, 558, L83
———. 2003, ApJ, 582, 60 (Paper II)
———. 2004, ApJ, 611, 685 (Paper VI)
Papovich, C., Dickinson, M., & Ferguson, H. C. 2001, ApJ, 559, 620
Pascarelle, S. M., Windhorst, R. A., & Keel, W. C. 1998, AJ, 116, 2659
Pettini, M., Kellogg, M., Steidel, C. C., Dickinson, M., Adelberger, K. L., & Giavalisco, M. 1998, ApJ, 508, 539
Pettini, M., Rix, S. A., Steidel, C. C., Adelberger, K. L., Hunt, M. P., & Shapley, A. E. 2002, ApJ, 569, 742
Pettini, M., Shapley, A. E., Steidel, C. C., Cuby, J., Dickinson, M., Moorwood, A. F. M., Adelberger, K. L., & Giavalisco, M. 2001, ApJ, 554, 981
Poli, F., Menci, N., Giallongo, E., Fontana, A., Cristiani, S., & D'Odorico, S. 2001, ApJ, 551, L45
Rudnick, G., et al. 2001, AJ, 122, 2205
Sawicki, M., & Yee, H. K. C. 1998, AJ, 115, 1329
Sawicki, M. J., Lin, H., & Yee, H. K. C. 1997, AJ, 113, 1
Schechter, P. 1976, ApJ, 203, 297
Schlegel, D. J., Finkbeiner, D. P., & Davis, M. 1998, ApJ, 500, 525
Shapley, A. E., Steidel, C. C., Adelberger, K. L., Dickinson, M., Giavalisco, M., & Pettini, M. 2001, ApJ, 562, 95
Shimasaku, K., et al. 2003, ApJ, 586, L111 (Paper IV)
Spergel, D. N., et al. 2003, ApJS, 148, 175
Steidel, C. C., Adelberger, K. L., Giavalisco, M., Dickinson, M., & Pettini, M. 1999, ApJ, 519, 1
Steidel, C. C., Adelberger, K. L., Shapley, A. E., Pettini, M., Dickinson, M., & Giavalisco, M. 2003, ApJ, 592, 728
Steidel, C. C., Giavalisco, M., Dickinson, M., & Adelberger, K. L. 1996a, AJ, 112, 352
Steidel, C. C., Giavalisco, M., Pettini, M., Dickinson, M., & Adelberger, K. L. 1996b, ApJ, 462, L17
Steidel, C. C., Hunt, M. P., Shapley, A. E., Adelberger, K. L., Pettini, M., Dickinson, M., & Giavalisco, M. 2002, ApJ, 576, 653
Steidel, C. C., Pettini, M., & Adelberger, K. L. 2001, ApJ, 546, 665
Sullivan, M., Treyer, M. A., Ellis, R. S., Bridges, T. J., Milliard, B., & Donas, J. 2000, MNRAS, 312, 442
Tresse, L., & Maddox, S. J. 1998, ApJ, 495, 691
Tumlinson, J., Giroux, M. L., Shull, J. M., & Stocke, J. T. 1999, AJ, 118, 2148
Vijh, U. P., Witt, A. N., & Gordon, K. D. 2003, ApJ, 587, 533
Wang, Y., Bahcall, N., & Turner, E. L. 1998, AJ, 116, 2081
Weinberg, D. H., Hernquist, L., & Katz, N. 2002, ApJ, 571, 15
Yagi, M., Kashikawa, N., Sekiguchi, M., Doi, M., Yasuda, N., Shimasaku, K., & Okamura, S. 2002, AJ, 123, 66
Yahata, N., Lanzetta, K. M., Chen, H., Fernández-Soto, A., Pascarelle, S. M., Yahil, A., & Puetter, R. C. 2000, ApJ, 538, 493
Yan, H., Windhorst, R. A., & Cohen, S. H. 2003, ApJ, 585, L93
Yan, L., McCarthy, P. J., Freudling, W., Teplitz, H. I., Malumuth, E. M., Weymann, R. J., & Malkan, M. A. 1999, ApJ, 519, L47